Draft version October 21, 2020
Typeset using LaTeX default style in AASTeX63

Atlas of CO-Line Shells and Cavities around Galactic Supernova Remnants with FUGIN*

Yoshiaki Sofue [1], Mikito Kohno [2] and Tomofumi Umemoto [3,4]

[1] Institute of Astronomy, The University of Tokyo, 2-21-1 Mitaka, Tokyo 181-8588, Japan
[2] Astronomy Section, Nagoya City Science Museum, 2-17-1 Sakae, Naka-ku, Nagoya, Aichi 460-0008, Japan
[3] Nobeyama Radio Observatory, National Astronomical Observatory of Japan (NAOJ), National Institutes of Natural Sciences (NINS), 462-2 Nobeyama, Minamimaki, Minamisaku, Nagano 384-1305, Japan
[4] Department of Astronomical Science, School of Physical Science, SOKENDAI (The Graduate University for Advanced Studies), 2-21-1 Osawa, Mitaka, Tokyo 181-8588, Japan

(Received 20xx; Revised 20xx; Accepted 20xx)

Submitted to AJ

ABSTRACT

Morphological search for molecular shells and cavities was performed around 63 Galactic supernova remnants (SNR) at $10^\circ \le l \le 50^\circ$, $|b| \le 1^\circ$using the FUGIN (FOREST Unbiased Galactic Imaging survey with the Nobeyama 45-m telescope) CO line data at high angular ($20''$) and velocity ($1.3\ \mathrm{km\ s^{-1}}$) resolutions. The results are presented as supplementary data for general purpose for investigations of the interaction between SNRs and interstellar matter in the form of an atlas of CO-line maps superposed on radio continuum maps at 20 cm along with a list of their kinematic distances determined from CO-line radial velocities.

Keywords: ISM, Supernova remnants — ISM, molecular cloud — catalogs — surveys

1. INTRODUCTION

Interaction between shock waves of supernova remnants (SNR) and molecular clouds (MC) has been a long-standing issue in the physics of the interstellar medium (ISM) (Chevalier 1977, 1999; Shull 1980; Lucas et al. 2020). The major concerns about the interaction are generation of interstellar turbulence (Kilpatrick et al. 2016), star formation (Seta et al. 2004), or suppression (McKee & Ostriker 1977; Cox et al. 1999), and cosmic ray acceleration (Fujita et al. 2009; Kuriki et al. 2018; Maxted et al. 2019).

Extensive observations of association of molecular clouds with well studied SNRs have been obtained in the last decades by molecular line observations (Tatematsu et al. 1990; Koo & Moon 1997; Tian et al. 2007; Ranasinghe & Leahy 2018). However, the current 'association' has been discussed mainly by coincidence of the distance of an SNR measued by some means with kinematic distance of the cloud from radial velocity, leaving large uncertainty. The association based on the morphological shell structure concentric to the SNR shock front has been obtained in few cases.

In this paper, we perform a systematic search for CO-line shells and/or cavities morphologically associated with Galactic SNRs listed in the Green's catalogue (http://www.mrao.cam.ac.uk/surveys/snrs) (Green 2009; Green & Dewdney 1992; Green 2019). We use ^{12}CO and ^{13}CO ($J = 1-0$) line channel maps from the FUGIN data set (Minamidani et al. 2016; Umemoto et al. 2017).

The purpose of this paper is to present the result in the form of an atlas of the identified molecular cavities and shells, and to provide with a finding chart for general purpose of the research of the interaction between SNR and ISM in the Galactic disc.

Corresponding author: Yoshiaki Sofue
sofue@ioa.s.u-tokyo.ac.jp

* FUGIN: FOREST (FOur beam REceiver System on the 45-m Telescope) Unbiased Galactic plane Imaging with the Nobeyama 45-m telescope

2. DATA

Table 1. Parameters of data sets

Telescope/Survey	Line/Band	Effective Resolution	Velocity Resolution	References
Nobeyama 45-m/FUGIN	^{12}CO $J = 1$–0	20″	1.3 km s^{-1}	Umemoto et al. (2017)[1]
	^{13}CO $J = 1$–0	21″	1.3 km s^{-1}	Umemoto et al. (2017)
VLA/VGPS	21 cm	$\sim$ 1′	—	Stil et al. (2006)[2]
VLA/MAGPIS	20 cm	$\sim$ 6″	—	Helfand et al. (2006)[3]
Effelsberg 100-m/Galactic Plane	21 cm	$\sim$ 9.4′	—	Reich et al. (1997)[4]

[1] http://nro-fugin.github.io
[2] http://www.ras.ucalgary.ca/VGPS/VGPS_data.html
[3] https://third.ucllnl.org/gps/index.html
[4] http://www3.mpifr-bonn.mpg.de/survey.html

Table B lists the SNRs from the Green's catalogue located in the FUGIN survey area at $10^\circ \le l \le 50^\circ$ and $|b| \le 1^\circ$ and $190^\circ \le l \le 230^\circ$. Figure 3 shows the positions of the SNRs on the color-coded maps of the peak $T_{\rm B}$ of the ^{12}CO , ^{13}CO , and C^{18}O line emission in the first Galactic quadrant (Umemoto et al. 2017). In order to compare the distributions of the CO line emission with radio distribution of the SNRs, we extracted 21 cm radio continuum maps of the SNRs from the archival web sites of the Multi-Array Galactic Plane Imaging Survey (MAGPIS: Helfand et al. (2006)), VLA Galactic Plane Survey (VGPS: Stil et al. (2006)), and the Effelsberg radio continuum survey (Reich et al. 1997). We summarize the parameters of data sets in Table 1.

The FUGIN project provided with high-sensitivity, high-spatial and velocity resolution, wide velocity (482 channels $\times$ 0.65 km s^{-1}) and wide field ($40^\circ \times 2^\circ$ along the Galactic plane from $l = 10^\circ$ to 50°) coverage by $(l, b, v_{\rm lsr} : T_{\rm B})$ cubes in the ^{12}CO , ^{13}CO and C^{18}O ($J = 1-0$) lines. The full beam width at half maximum of the telescope was 15″at the ^{12}CO ($J = 1-0$)-line frequency, and the velocity resolution was 1.3 km s^{-1}. The effective beam size of the final data cube was 20″, and the rms noise levels were ~ 1 K. The final 3D FITS cube had a voxel size of $(\Delta l, \Delta b, \Delta v_{\rm lsr}) =$ (8.5″, 8.5″, 0.65 km s^{-1}), which are available as the archival data.

3. ATLAS

We present the atlas of molecular cavities, shells and partial arcs apparently surrounding the SNRs by superposition of ^{12}CO channel maps on radio continuum maps at 20 cm.

The search for a CO shell associated with a SNR was done by the following procedure. Since the distance of a SNR is unknown, or uncertain even if it exists, so that its radial velocity is not known, the search for the shell structure was done in all the 462 channels of the CO data cube from -100 to 200 km s^{-1}by one channel after another for each SNR.

First we present the radio continuum image on the screen, and then superpose a channel map ($T_{\rm B}$ map) on the same screen. Then, the CO channel is changed from 1st to 462nd step by step. Numerous CO clouds and filaments will pass by, mostly fore- and background emissions, but at a certain velocity channel, a possible shell/cavity/arc appears apparently associated with the SNR's shell edge.

Once such a candidate was found, its nearby channels are inspected more carefully, and the clearest shell feature was chosen as the associated shell, and its channel velocity was adopted as the radial velocity of the shell. This was repeated in ^{12}CO and ^{13}CO cubes, each 462 channels, for all the 63 SNRs. C^{18}O data were not used for their too weak emission.

Table B lists the positions, radial velocities, kinematic distances and linear diameters of the candidates cavities and/or shells of the analyzed SNRs. The measured results are presented by $T_{\rm B}$ maps (sometimes $I_{\rm CO}$ maps) in the ^{12}CO line emission of the CO shells, arcs, and/or concentric alignment of clumps, as superposed on 20-cm radio continuum maps. We also present superposed ^{13}CO and ^{12}CO maps by R (red) and G (green) color-coded images in order to examine the degree of condensation of the molecular gas density. The result is presented as an atlas in the figures of Appendix.

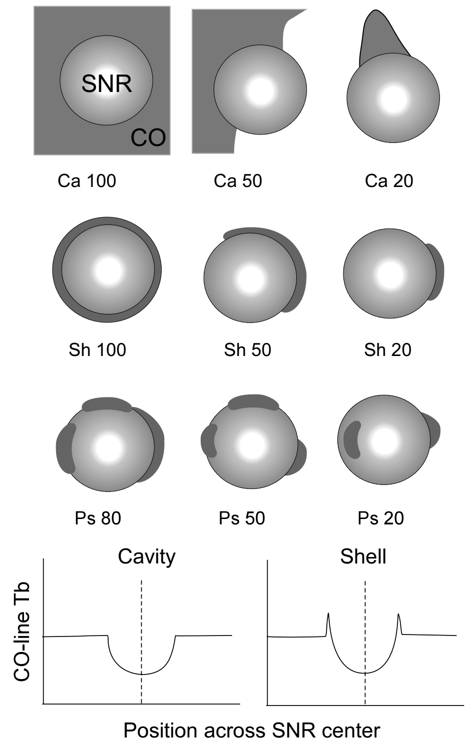

Figure 1. Shell types and shell measure .

3.1. *Morphological classification*

SNR interacting with a molecular cloud will deform the cloud to make a concave boundary with respect to the SNR center. Thereby, the resulting cloud morphology will depend on the extent and density of the cloud. We categorize the structure of a shell or a cavity of the CO brightness distribution apparently surrounding a SNR as follows:

i) Cavity (Ca κ): When the cloud is extended more largely than the SNR size or comparable, a round cavity is created around the SNR due to dissociation of molecular gas and accumulation at the shock front. If the cloud size is sufficiently large, the cavity will be fully embedded in the cloud, making a round shape on the sky. We define such a case a cavity with completeness of 1 or 100%, and introduce a completeness parameter or the shell measure, $\kappa = 1$. If the cloud size is comparable or smaller, the dissociation and/or compression will take place partially, forming open cavity to the inter-cloud space. Such a partial cavity may be categorized by its completeness or shell measure with $\kappa < 1$, depending on the fraction of the boundary from a perfect loop.

ii) Shell (Sh κ): If the cloud's density is lower, the gas will be accumulated or snow-plowed around the shock front, making a shell structure. The shell may be categorized by its completeness from $\kappa = 1$ showing a perfect loop, or partial loops with $\kappa < 1$.

iii) Partial/clumpy shell (Ps=Cs κ): Clouds are often more turbulent and clumpy. In such a case, the interaction front will produce more partial features such as a clumpy shell or an ensemble of partial arcs. We categorize such a case by the fraction of the total partial arcs compared to a round loop by a factor of κ.

Figure 1 illustrates typical morphology of the CO brightness distribution around a SNR.

Description of properties of the obtained maps are given in figure captions of individual objects in the atlas. We here present an example for G11.18-0.35+32.975 km s^{-1}in figure 2. This SNR is a typical bright shell in radio continuum, and its western half is apparently contacting, on the sky, with a half-cavity of a CO line cloud. The RGB image indicates that the edge of the cavity facing the SNR does not show a signature of strong compression of gas, which would cause a red-color (^{13}CO) excess, if it existed. Therefore, despite of the excellent coincidence of the concave edge of the CO cloud with the SNR's outer edge, physical association cannot be proved from the present analysis.

3.2. *Distances*

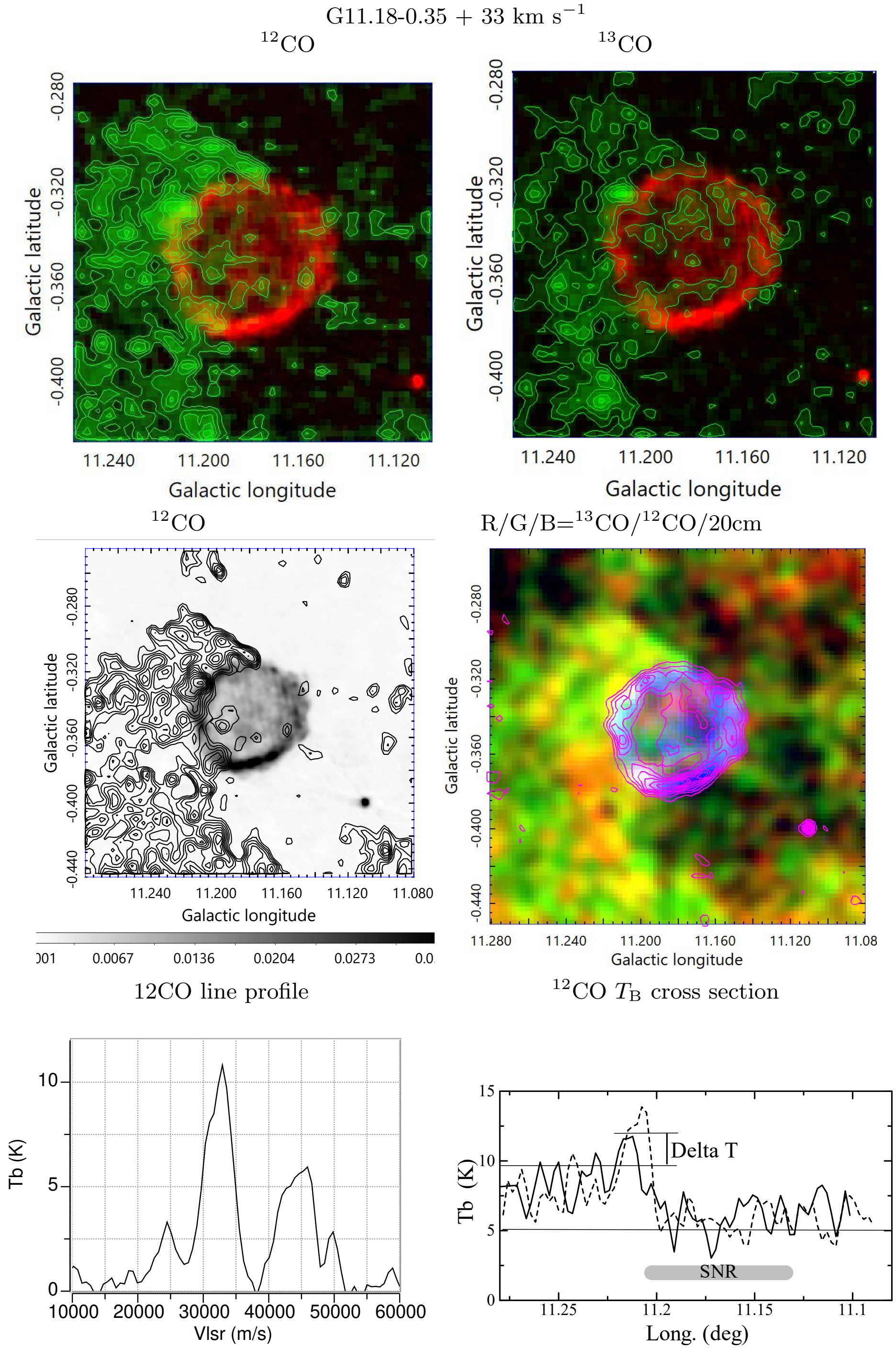

Figure 2. Example of molecular cavity/shell of Ca/Sh 50 toward SNR G11.18-0.35 at $v_{\rm lsr} = +32.925$ km s^{-1}by (tl) ^{12}CO contours from 7 K every 1 K on 20 cm in red; (tr) ibid, 7 K every 0.5 K, superposed on a grey-scale map of 20 cm radio continuum from 0 to 0.03 Jy beam^{-1} ; (ml) CO from 2 K every 1 K; (mr) RGB color coded images of ^{13}CO (red: auto), ^{12}CO (green: auto) and 20 cm (blue: auto, magenta contour interval by 5 mJy beam^{-1}), (bl) ^{12}CO line spectrum at the western edge; (br) ^{12}CO $T_{\rm B}$ across the SNR center along $b = -0.34°$ (dash) and $-0.36°$ (full line), showing the 'cavity' property. All figures of the studied SNRs are presented in the electronic supplementary data described in the text.

The radial velocity, $v_r = v_{\rm lsr}$, at a distance r orbiting around the Galactic Center is related to the circular rotation velocity $V(R)$ as a funciton of the galacto-centric distance R as

$$v_r = \left(\frac{R_0}{R}V(R) - V_0\right)\sin\ l, \tag{1}$$

where R is the galacto-centric distance related to r and galactic longitude l by

$$r = R_0 \cos\ l \pm \sqrt{R^2 - R_0^2 {\rm sin}^2 l}. \tag{2}$$

We assume here $V_0 = 238$ km s^{-1}and $R_0 = 8.0$ km s^{-1}(Honma et al. 2015),and adopt the recent rotation curve derived by compilation of determined circular velocities in the last two decades (Sofue 2020). Here, we approximate the rotation curve by an analytic expression,

$$V(R) = \left(\frac{V_1}{[1+(R/a)^2]^{1/2}} + \frac{V_2}{1+(R/b)^2}\right)R. \tag{3}$$

Here, the parameters, $V_1 = 67$, $V_2 = 1000$ km s^{-1}, $a = 3.5$ kpc, $b = 0.44$ kpc, were determined by iterative fitting of the function to the data by trial and error, until one gets satisfactory reproduction of the data within radius range, 1.4 to ~ 10 kpc, necessary for the present analysis.

For a given set of $v_{\rm r}$ and l, we can determine R by iteration using equations 1 and 3, and the distance r is obtained by equation 2. In table B we list the determined distances and radii of the SNR. The errors are calculated using the uncertainty of radial velocity of the CO line in the measured value as well as the interstellar turbulence, $\delta v_{\rm lsr} \sim 5$ km s^{-1}, and the uncertainty in the rotation velocity, $\delta V_{\rm rot} \sim 5$ km s^{-1}, propagating through the above equations to r. The uncertainties in R_0 and V_0 are not included.

3.3. *Molecular mass*

The molecular mass of associated clouds is one of the most essential quantities. However, the present resolution, $20'' \sim 0.5$ pc at 5 kpc for example, is a few orders of magnitudes wider than the expected thickness of shock-compressed filaments at the SNR fronts (Lucas et al. 2020). So, we are not able to estimate meaningful mass of the directly associated molecular gas to the SNRs.

Instead, we here try to estimate the upper limit to the associated cloud for G11.17-0.35 as a typical example. Measuring the excess $T_{\rm B}$ at the edge of the SNR over that in the ambient emission outside SNR, the upper limit mass may be calculated by

$$M \sim \mu\ m_{\rm H}\ 2\pi\kappa R_{\rm s}\ \delta R_{\rm beam} X_{\rm CO} \int \delta T dv, \tag{4}$$

where $\mu \sim 2.6$ is the reduced mass per H_2 molecule for solar abundance, $m_{\rm H}$ is the hydrogen mass, $X_{\rm CO} \sim 2 \times 10^{20}$ cm^{-2} [K km s^{-1}]$^{-1}$ (Sofue & Kohno 2020) is the conversion factor, $R_{\rm S}$ is the SNR radius, $\delta R_{\rm beam} = \theta_{\rm beam} r$ is the beam width at the object, κ is the cavity/shell measure, and δT is the excess brightness temperature of ^{12}CO line at the intensity peak along the shell or the edge of cavity contacting the SNR.

For G11.17-0.35 at 33 km s^{-1}(figure 2), we obtain $\delta T \sim 5$ K and $\kappa \sim 0.5$, and the possibly associated molecular mass is shown to be $M <\sim 10^2$ and $<\sim 10^3 M_\odot$ for the near and far distances, respectively. Similar estimation applies to most of the observed partial CO shells in the analyzed SNR, but we do not present the results for individual objects, because the estimations are simply upper limits to the physically meaningful masses, which are supposed to be a few orders of magnitudes smaller, as discussed above.

4. SUMMARY

We obtained a systematic search by morphology for cavity and/or shell structures of ^{12}CO and ^{13}CO line emissions adjacent to 63 catalogued Galactic SNRs. Such a search was possible only by careful inspection of individual channel maps of brightness temperature with high-velocity and high-angular resolutions from the FUGIN CO survey. The result is presented in the form of a table of kinematical distances of the CO shells, and an atlas of CO-line $T_{\rm B}$ maps as superposed on the radio continuum maps of the SNRs, which will be useful for general purpose for the investigation of the interaction between SNRs and ISM in the Galaxy.

ACKNOWLEDGMENTS

We are grateful to Prof. Masumichi Seta of Kwansei Gakuin University and Dr. Hidetoshi Sano of the National Astronomical Observatory of Japan for helpful advises, and to Mr. Yuya Tsuda of Meisei University for discussion. The CO data were taken from the FUGIN CO survey obtained with the Nobeyama 45-m telescope, and retrieved from the JVO portal (http://jvo.nao.ac.jp/portal). The data analysis was carried out at the Astronomy Data Center of the National Astronomical Observatory of Japan. Radio continuum data were taken from the VGPS survey via the ATLASGAL data archives. The National Radio Astronomy Observatory is a facility of the National Science Foundation operated under cooperative agreement by Associated Universities, Inc.. This research is supported as part of the International Galactic Plane Survey through a Collaborative Research Opportunities grant from the Natural Sciences and Engineering Research Council of Canada.

Facilities: Nobeyama 45-m, VLA, Effelsberg 100-m

Software: astropy (Astropy Collaboration et al. 2013)

REFERENCES

Astropy Collaboration, Robitaille, T. P., Tollerud, E. J., et al. 2013, A&A, 558, A33

Chevalier, R. A. 1977, ARA&A, 15, 175

Chevalier, R. A. 1999, ApJ, 511, 798

Cox, D. P., Shelton, R. L., Maciejewski, W., et al. 1999, ApJ, 524, 179

Deharveng, L., Schuller, F., Anderson, L. D., et al. 2010, A&A, 523, A6

Fujita, S., Torii, K., Tachihara, K., et al. 2019, ApJ, 872, 49

Fujita, Y., Ohira, Y., Tanaka, S. J., et al. 2009, ApJL, 707, L179

Green, D. A. 2009, Bulletin of the Astronomical Society of India, 37, 45

Green, D. A., & Dewdney, P. E. 1992, MNRAS, 254, 686

Green, D. A. 2019, Journal of Astrophysics and Astronomy, 40, 36

Helfand, D. J., Becker, R. H., White, R. L., et al. 2006, AJ, 131, 2525

Honma, M., Nagayama, T., & Sakai, N. 2015, PASJ, 67, 70

Kilpatrick, C. D., Bieging, J. H., & Rieke, G. H. 2016, ApJ, 816, 1

Koo, B.-C., & Moon, D.-S. 1997, ApJ, 485, 263

Kuriki, M., Sano, H., Kuno, N., et al. 2018, ApJ, 864, 161

Lucas, W. E., Bonnell, I. A., & Dale, J. E. 2020, MNRAS, 493, 4700

Maxted, N. I., Filipović, M. D., Hurley-Walker, N., et al. 2019, ApJ, 885, 129

McKee, C. F., & Ostriker, J. P. 1977, ApJ, 218, 148

Minamidani, T., Nishimura, A., Miyamoto, Y., et al. 2016, Proc. SPIE, 99141Z

Ranasinghe, S. & Leahy, D. A. 2018, MNRAS, 477, 2243

Reich, P., Reich, W., & Furst, E. 1997, A&AS, 126, 413

Seta, M., Hasegawa, T., Sakamoto, S., et al. 2004, AJ, 127, 1098

Shull, J. M. 1980, ApJ, 237, 769

Sofue, Y. 2020, Galaxies, 8, 37

Sofue, Y. & Kohno, M. 2020, MNRAS, 497, 1851

Stil J. M., et al., 2006, AJ, 132, 1158

Tatematsu, K., Fukui, Y., Landecker, T. L., et al. 1990, A&A, 237, 189

Tian, W. W., Leahy, D. A., & Wang, Q. D. 2007, A&A, 474, 541

Umemoto, T., Minamidani, T., Kuno, N., et al. 2017, PASJ, 69, 78

APPENDIX

A. SNR DISTRIBUTION

Figure 3 shows the positions of the SNRs from the Green's catalogue on the CO line brightness map (red: ^{13}CO, green: ^{12}CO, blue: C^{18}O).

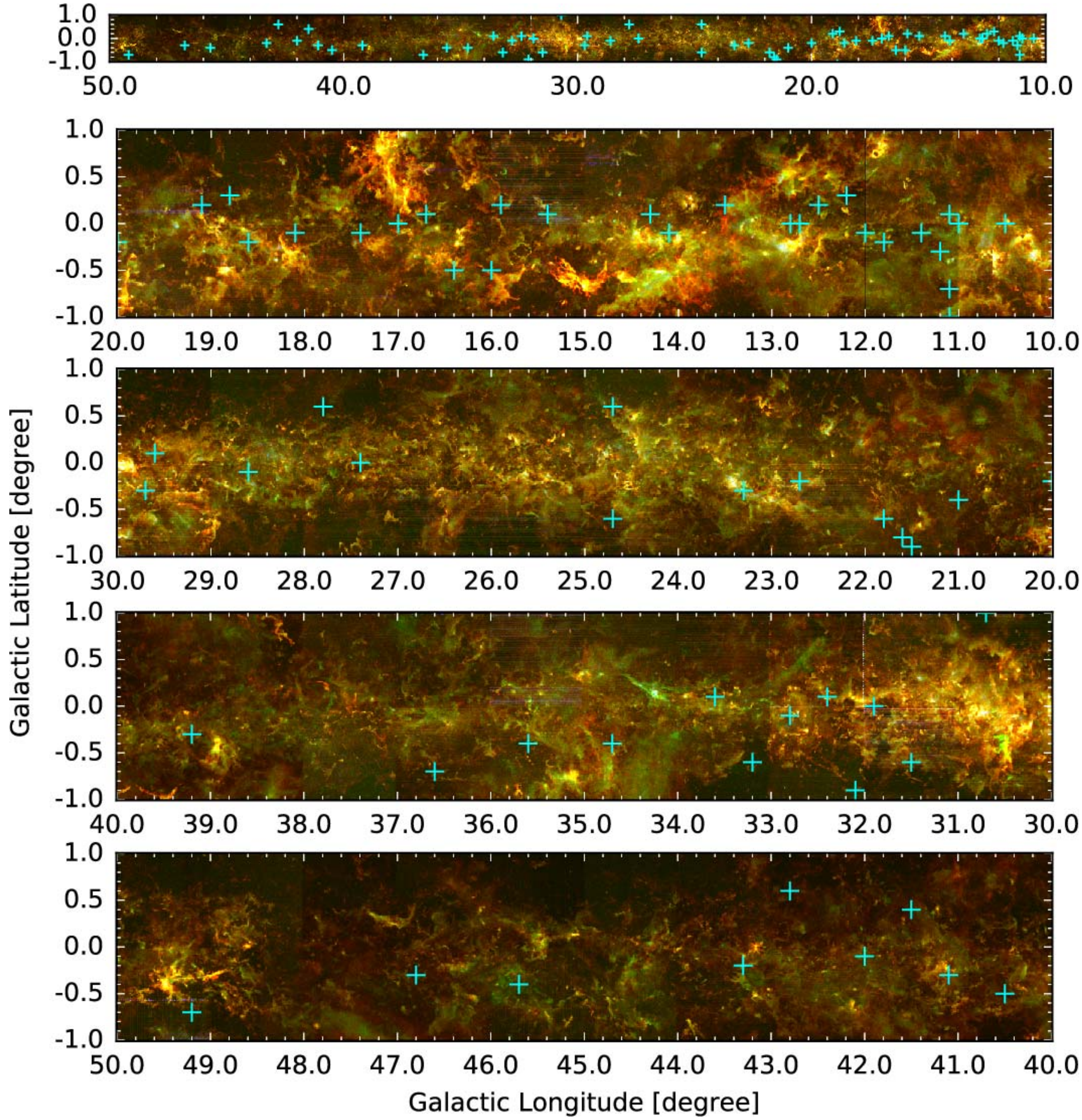

Figure 3. Green's SNRs (crosses) superposed on the FUGIN CO map (https://nro-fugin.github.io) of the peak brightness temperatures of ^{12}CO, ^{13}CO and C^{18}O lines in red, green and blue, respectively (Umemoto et al. 2017).

B. TABLE OF SNRS

Table B lists the analyzed objects and derived parameters for the candidate CO line features adjacent to the SNRs.

Table 2. CO-line cavities and shells toward SNRs from the Green's catalogue.

(a)	(b)	(c)	(d)	(e)	(f)	(g)	(h)	(i)	(j)	(k)	(l)	(m)
l, b	$v_{\rm lsr}$	Size	SNR	$f_{\rm 1GHz}$	Sp.I.	Type†	$r_{\rm near}$	$r_{\rm far}$	δr	$D_{\rm near}$	$D_{\rm far}$	Name
(°,°)	(km/s)	(′×′)	type	(Jy)		(κ in %)	(kpc)			(pc)		
11.00-0.05	+40	11 9	S	1.3	0.6	Sh 50	6	11.6	0.3		12.0	33.4
11.1-0.7	+33	11 7		1.0	0.7	Ps 50	3.5	12.2	0.3	8.9	31.2	
(11.1 +0.1)	—	12 10	S	2.3	0.4	N						
11.17-0.35	+33	4 4	C	22	0.5	Ca 50	3.7	12.0	0.3	4.3	14.0	
11.2+0.12	+56	12 10	S	2.3	0.4	Ps 30	6	10.8	0.2	11.6	25.7	
11.4-0.1	+30	8 8	S?	6	0.5	Ca 60	3.4	12.3	0.3	8.0	28.5	
—	+50					Ca 50	4.1	11.5	0.3	9.6	26.9	
11.89-0.23	+49.8	4 4	F	0.7	0.3	Ca 50	4.5	11.1	0.2	5.3	13.0	
12.0 -0.1	+37.4	7 7 ?	?	3.5	0.7	Ps 50	3.8	11.8	0.3	7.7	24.1	
(12.2 +0.3)	—	6 5	S	0.8	0.7	N						
(12.5 +0.2)	—	6 5	C?	0.6	0.4	N						
(12.7 -0.0)	—	6	S	0.8	0.8	N						
(12.8 -0.0)	—	3	C?	0.8	0.5							
13.45+0.14	+24	5 4	S	3.5?	1.0?	Ca 50	2.7	12.9	0.2	3.5	16.8	
(14.1 -0.1)	—	6 5	S	0.5	0.6	N						
(14.3 +0.1)	—	5 4	S	0.6	0.4	N						
15.42+0.16	+34	15 14	S	5.6	0.62	Sh 60	3.2	12.3	0.3	13.3	51.7	
15.9+0.2	+29	7 5	S?	5.0	0.63	Ps 50	2.8	12.6	0.3			
(16.0 -0.5)	—	15 10	S	2.7	0.6	N						
(16.4 -0.5)	—	13 13	S	4.6	0.3?	N						
16.75+0.08	+47	4 4	C	3.0	0.6	Ca 90	3.8	11.6	0.3	4.4	13.5	
—	+62					Ps 50	4.5	10.9	0.2	5.2	12.6	
17.05-0.05	+31.0	6 6	S	0.4	0.7	Ca 50	2.8	12.5	0.3	4.1	18.2	
—	+93.4	6 6	S	1.4	0.4	Ca 30	5.6	9.7	0.2	8.2	14.1	
18.1-0.1	+49	8 8	S	4.6	0.5	Ps 50	3.7	11.5	0.3	8.7	26.7	
18.6 -0.2	+66	6 6	S	1.4	0.4	Ca 50	4.5	10.7	0.2	7.8	18.7	
18.8+0.35	+ 20	17 11	S	33	0.46	Ps 60	1.9	13.3	0.4	7.4	52.8	Kes 67
(19.1 +0.2)	—	27 27	S	10	0.5	N						
20.0-0.2	+65	10 10	F	10	0.1	Ca 60	4.3	10.7	0.2	12.6	31.2	
(20.4 +0.1)	—	8 8	S?	9?	0.1?	N						
(21.0 -0.4)		9 7	S	1.1	0.6	N						
(21.5 -0.9)	–	5 5	C	7 var		No 20cm						
(21.6-0.8)		13	S	1.4	0.5?	No 20cm						
21.8-0.6	+83	20 20	S	65	0.56	Sh 70	5.0	9.9	0.2	28.9	57.6	Kes 69
22.7-0.2	+75	26 26	S?	33	0.6	Ps 60	4.6	10.2	0.2	34.7	76.9	
23.3-0.3	+70	27 27	S	70	0.5	Ps 70	4.3	10.4	0.2	34.1	81.3	W41
(23.6 +0.3)	—	10 10	?	8?	0.3	N						
24.7-0.6	+60	15 15	? S?	8	0.5	Ca 30	3.8	10.7	0.3	16.7	46.7	
24.7+0.6	+112	30 15	C?	20?	0.2?	C/P 60	6.3	8.2	0.4	39.1	50.6	

† "N" means that no possible cavity/shell in CO was recognized.

Columns: (a) Galactic position; (b) CO line radial velocity; (c) apparent major and minor-axis sizes, θ_x, θ_y; (d) SNR type; (e) radio flux at 1 GHz; (f) spectral index; (g) CO cavity or shell measure; (h) near solution of the distance; (i) far distance; (j) distance error; (k)linear diameter for near distance $D = \sqrt{\theta_x \theta_y} r$; (l) for far distance, (m) Name. Columns (Authors),(c),(d),(e),(f) and (q) are from Green's catalogue.

Table 2. Continued.

l, b (°,°)	$v_{\rm lsr}$ (km/s)	Size (′×′)	SNR type	$f_{\rm 1GHz}$ (Jy)	Sp.I.	Type (κ in %)	$r_{\rm near}$ (kpc)	$r_{\rm far}$	δr	$D_{\rm near}$ (pc)	$D_{\rm far}$	Name
27.4+0.0	+101	4 4	S	6	0.68	Ca 60	5.8	8.4	0.4	6.8	9.8	4C-04.7
(27.8 +0.6)	—	50 30	F	30 var		N						
28.62-0.10	+86	13 9	S	3?	?	Ca 60	5.0	9.0	0.3	15.7	28.5	
29.6 +0.1	+99.2	5	S	1.5?	0.5?	Sh 50	5.9	8.0	0.5	8.6	11.7	
29.70-0.26	+52	3 3	C	10	0.63	Ca 50	3.3	10.6	0.3	2.9	9.3	Kes 75
—	+112					Ps 40	3.3	10.6	0.3	2.9	9.3	
31.5-0.6	+87.5	18 18?	S?	2?	?	Ps 50	5.2	8.4	0.3	27	44	
—	+97					Ca 40	6.0	7.6	0.5	31	40	
31.9+0.0	+107	7 5	S	25 var		Ca 50	6.8	6.8	–	12	12	3C391
32.1-0.9	+95	40 40?	C?	?	?	N	5.9	7.7	0.5	69	89	
32.4+0.1	+10.8	6 6	S	0.25?	?	Ca 100	0.79	12.7	0.2	1.4	22	
—	+42.6					Ca 30	2.7	10.8	0.2	4.8	18.8	
32.8 -0.1	+74	17 17	S?	11?	0.2?	Ps 10	4.4	9.0	0.25	22	45	Kes 78
—	+103					Ca 30	6.7	6.7	–	33	33	Kes 78
33.2 -0.6	+54	18 18	S	3.5 var		Ps 20	3.3	10.1	0.2	17	53	
—	+91					Ca 10	5.7	7.7	0.5	30	40	
33.7+0.05	+70	10 10	S	20	0.51	Ca 70	4.2	9.1	0.3	12.3	26.4	Kes 79
34.7-0.4	+40	35 27	C	250	0.37	Ca 60	2.6	11	0.2	23	95	W44
—	+52					Ca 75	3.2	9.9	0.2	29	89	W44
35.6 -0.4	+55	15 11	S?	9	0.5	Ca 40	3.4	9.6	0.2	13	36	
—	+90					Pa 20	6.5	6.5	–	24	24	
36.6-0.7	+57	25 25?	S?	1.0	0.7?	Ca 20	3.5	9.3	0.3	26	68	
—	+79					Ca 20	5.1	7.8	0.4	37	57	
39.2-0.3	+51	8 6	C	18	0.34	Ca 30	3.2	9.2	0.3	6.5	18.5	3C396
—	+67					Ca 60	4.3	8.1	0.5	8.7	16.2	
40.5 -0.5	+58	22 22	S	11	0.4	Ca 70	3.8	8.4	0.3	24	54	
41.1 -0.3	+32	4.5 2.5	S	25	0.50	Ca 60	2.1	10.0	0.3	2.0	9.7	3C397
—	+38					Ca100	2.5	9.6	0.3	2.4	9.4	
41.5+0.4	+58	10 10	S?	1?	?	Ca 50	3.8	8.2	0.4	11	24	
42.0-0.1	+66	8x8	S?	0.5?	?	Ca 60	4.6	7.3	0.5	11	17	
(42.8 +0.6)		24 24	S	3?	0.5?	N						
43.3-0.2	+10	4 3	S	38	0.46	Ca 50	0.7	11	0.3	0.7	11	W49B
—	+45					Ca 60	3.0	8.7	0.3	3.0	8.7	W49B
—	+62					Ca 100	4.4	7.3	0.7	4.4	7.3	W49B
45.7 -0.4	+26	22 22	S	4.2?	0.4?	Pa 40	1.8	9.4	0.3	11	60	
—	+48.5					Pa 20	3.4	7.8	0.4	22	50	
46.8-0.3	+52	15	S	17	0.54	Ca 70	3.9	7.1	0.5	17	31	HC30
49.2 -0.7	+50	30 30	S?	160?	0.3?	Pa 30	4.1	6.4	0.7	35	56	W51C
—	+60	30 30	S?	160?	0.3?	Ca 50	5.2	5.2	–	46	46	W51C
205.5 +0.5	+10	220	S	140	0.4	N	0.98	—	0.3	63	—	Monoceros
—	+20					N	2.2	—	0.3	139	—	Monoceros
213.0 -0.6	+9	160x140?	S	21	0.4	N	0.7	—	0.3	32	—	
—	+21					N	1.8	—	0.3	80	—	

G11.00-0.05+40 km s^{-1}

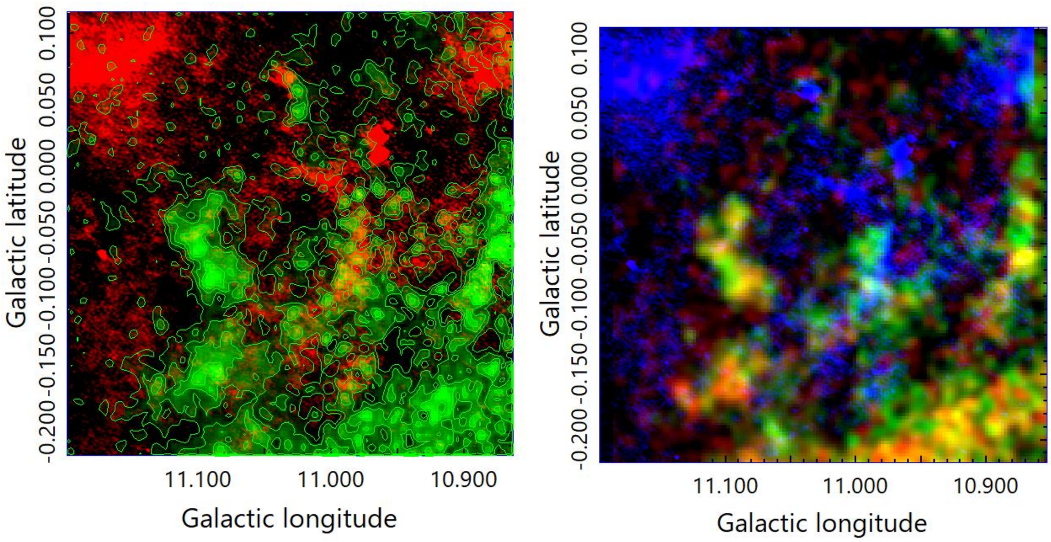

Figure 4. Same as figure 2, but for SNR G11.00-0.05+40.725, 40.075 km s^{-1}: (Left) ^{12}CO contours superposed on the radio continuum map in red. Contours start at 2K by step 1K. (Right) Two color composite image of CO T_{B}, red and green showing ^{12}CO and ^{13}CO respectively, superposed on 20-cm radio map.

G11.1-0.7, +33.6 km s^{-1}

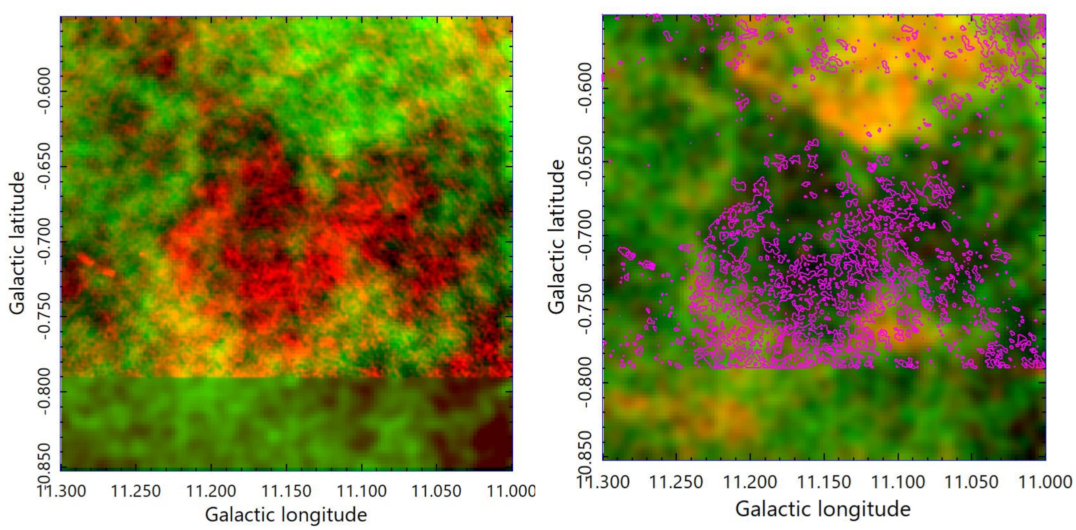

29.025 km s^{-1}

Figure 5. Same as figure 2, but for SNR G11.1-0.7, 33 km s^{-1}: (Left) ^{12}CO T_{B} in green (from 0 to 10 K) superposed on 20 cm brightness map in red. (Right) Composite CO map of co and ^{13}CO T_{B} (R(^{13}CO, 0 - 4K), G(^{12}CO, 0 - 12K)) on radio 20-cm contour map (from 0.5, step 0.5 mJy beam^{-1} .

C. FIGURES

Figures 4 to 50 show the analyzed results on individual SNRs.

G11.17-0.35+33 km s^{-1}

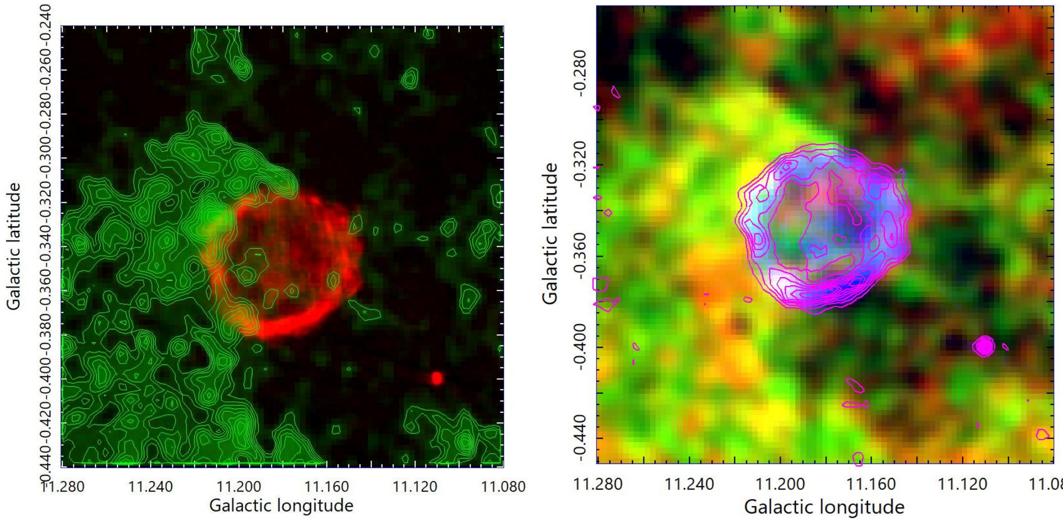

Figure 6. Same as figure 2, but for SNR G11.18-0.35+32.925km s^{-1}: (Left) ^{12}CO contour map (from 7K by 0.5K) superposed on 20cm radio in red color. (Right) Two-color map of ^{12}CO in green and ^{13}CO in red superposed on the 20-cm contour map (start 5, step 5 mJy beam^{-1}).

G11.2+0.12+55 km s^{-1}

55.025 56.975 km s^{-1}

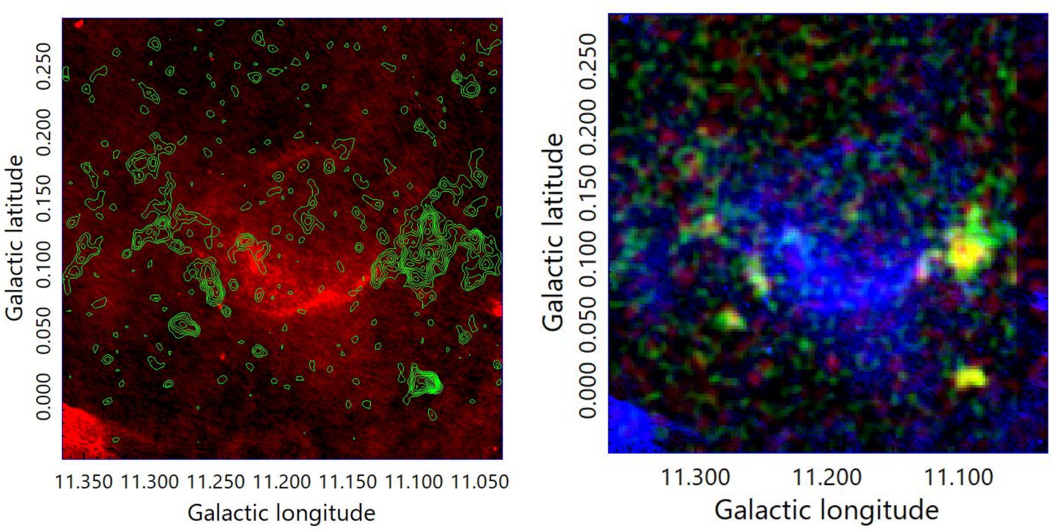

Figure 7. Same as figure 2, but for SNR G11.2+0.12+55 km s^{-1}. (Left) ^{12}CO $T_{\rm B}$ contour map (start 2K, step 2K) superposed on 20-cm radio continuum map in red (0 to 3 mJy beam^{-1}). (Right) Two-color CO $T_{\rm B}$ map (^{12}CO in green (0 to 8 K), ^{13}CO in red (0 to 2.5 K)) superposed on 20-cm map in blue (from 0.5 to 2 mJy beam^{-1}).

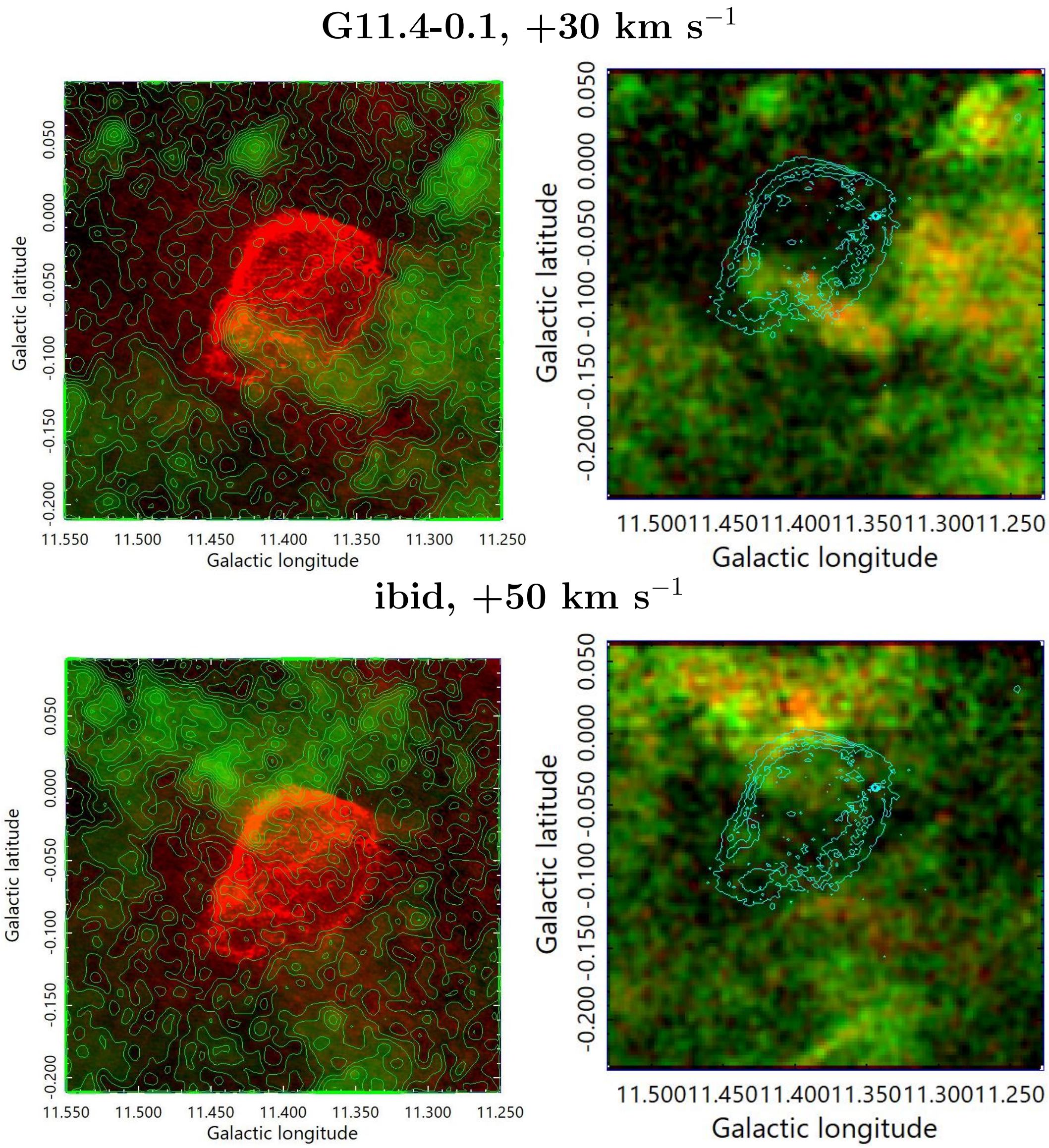

Figure 8. Same as figure 2, but for SNR G11.4-0.1+30.325, +49.875 km s^{-1}: (Left) ^{12}CO contours (start at 1K, step 1K) superposed on 20 cm radio map in red. (Right) ^{13}CO in red color (0 to 5K) and ^{12}CO in green (0 to 10K), superposed on 20 cm contour map from (0.5 to 2 mJy beam^{-1}).

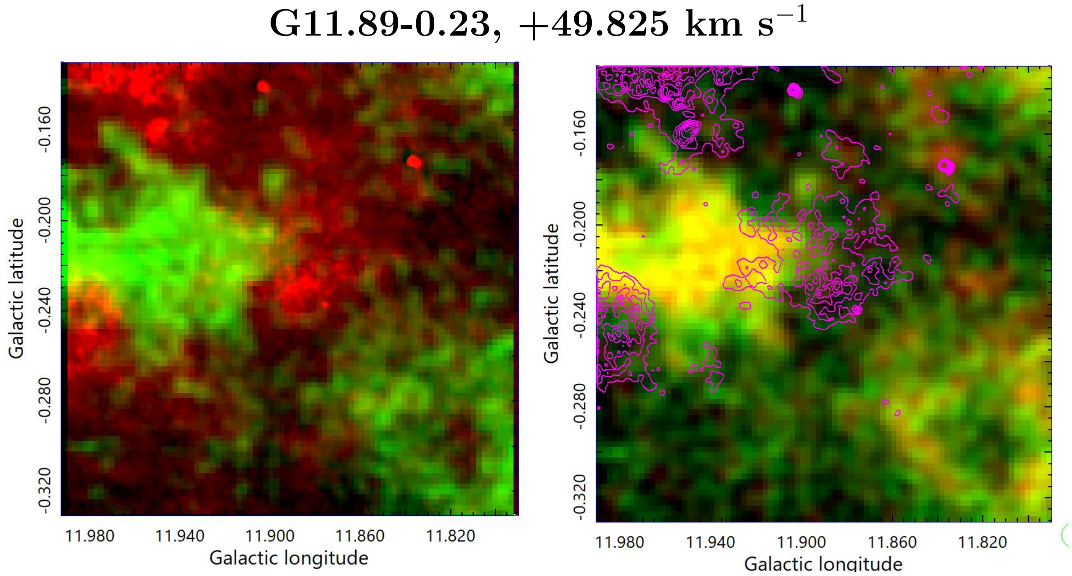

Figure 9. Same as figure 2, but for SNR G11.89-0.23, +49.825 km s^{-1}, ^{13}CO R(0-3K), ^{12}CO G(0-10K), cont.(start 1.5 step 0.5 mJy beam^{-1}).

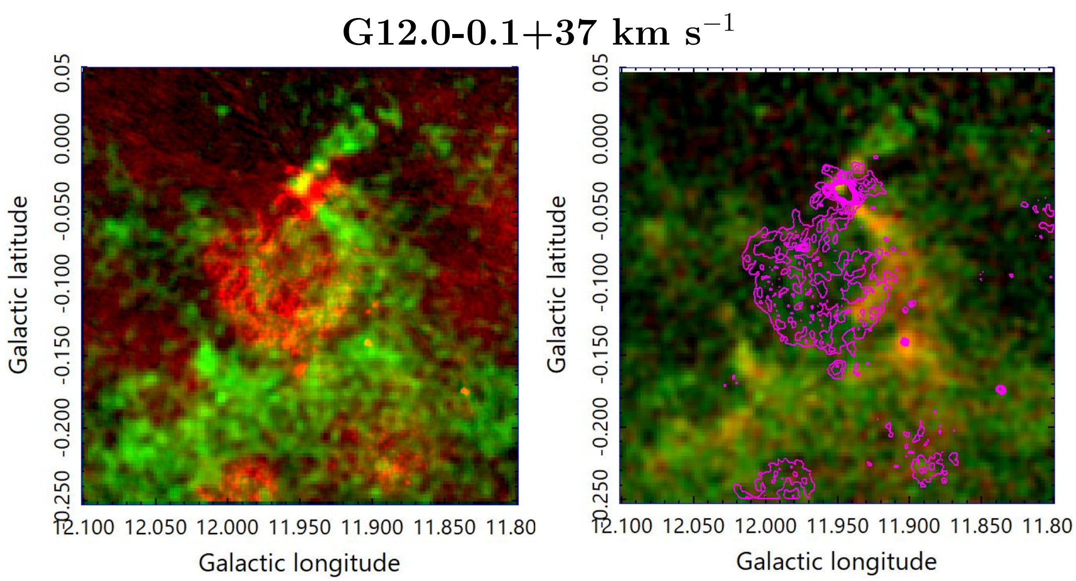

Figure 10. Same as figure 2, but for SNR G12.0-0.1+37, +37.475 km s^{-1}, ^{13}CO R(0-6K), ^{12}CO G(0-15K), 20cm cont. start 2 step 2 mJy beam^{-1}).

G13.45+0.14+24 km s^{-1}

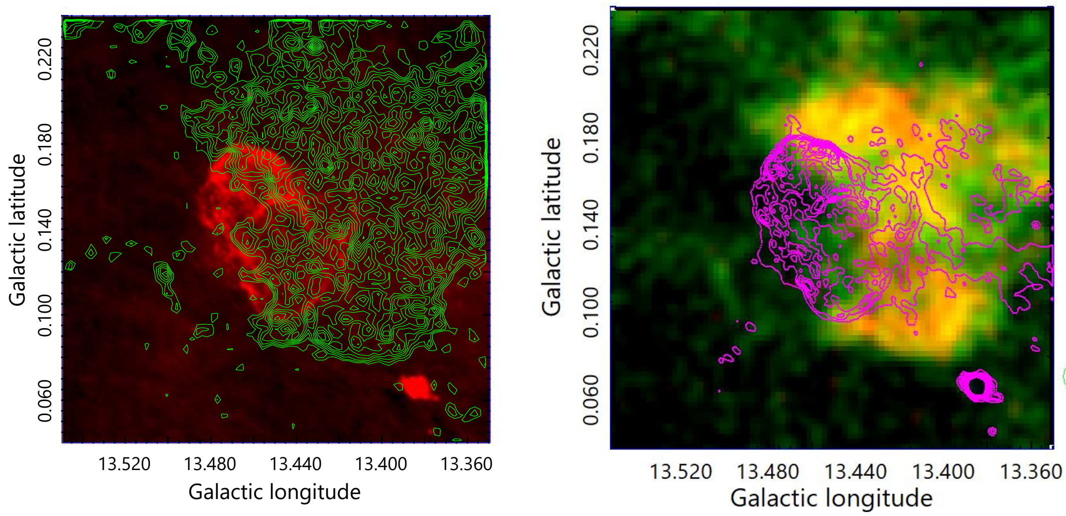

Figure 11. Same as figure 2, but for SNR G13.45+0.14+24 km s^{-1}; ^{12}CO start 5K step1 K; 20cm start 0 step 7 mJy beam^{-1} . R(1-5K)/G(1-15K)/Cont(2by1mJy), 24.475 km s^{-1}

G15.42+0.16+34 km s^{-1}

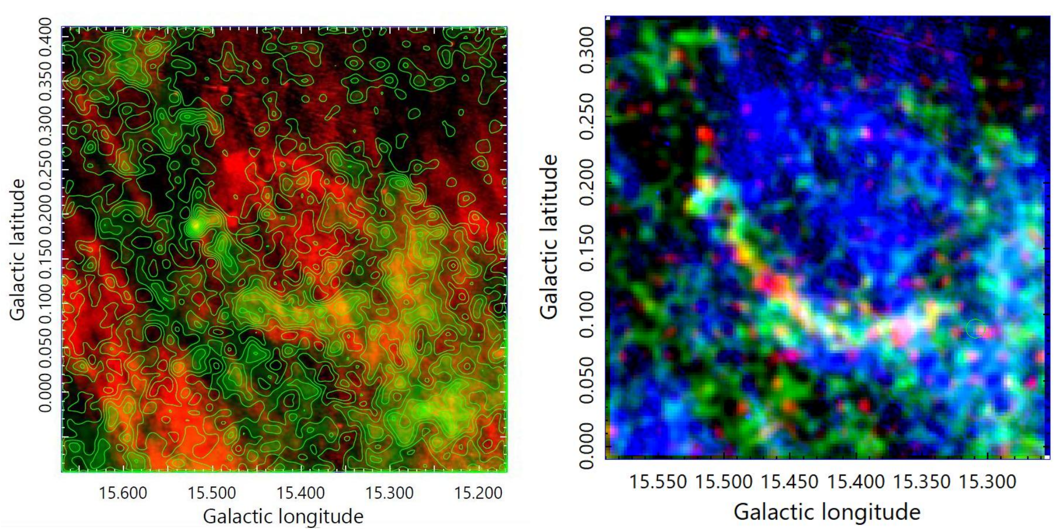

Figure 12. Same as figure 2, but for SNR G15.42+0.16, 34.225 km s^{-1}:, ^{12}CO contours start at 1K with step 1K.

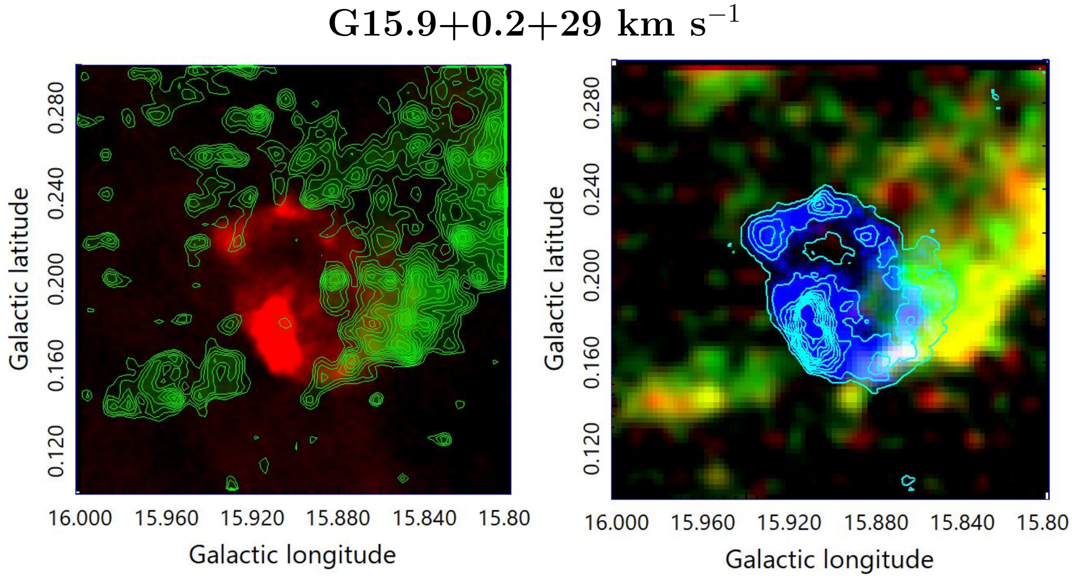

Figure 13. Same as figure 2, but for SNR G15.9+0.2+29. (Left) ^{12}CO contours start at 5 K by step 1 K superposed on 20 cm in red (0 - 5 mJy beam^{-1}). (Right) R(^{13}CO 0.5-4K) / G(^{12}CO 2-12K)/ B(20 cm contours 0-8mJy beam^{-1}).

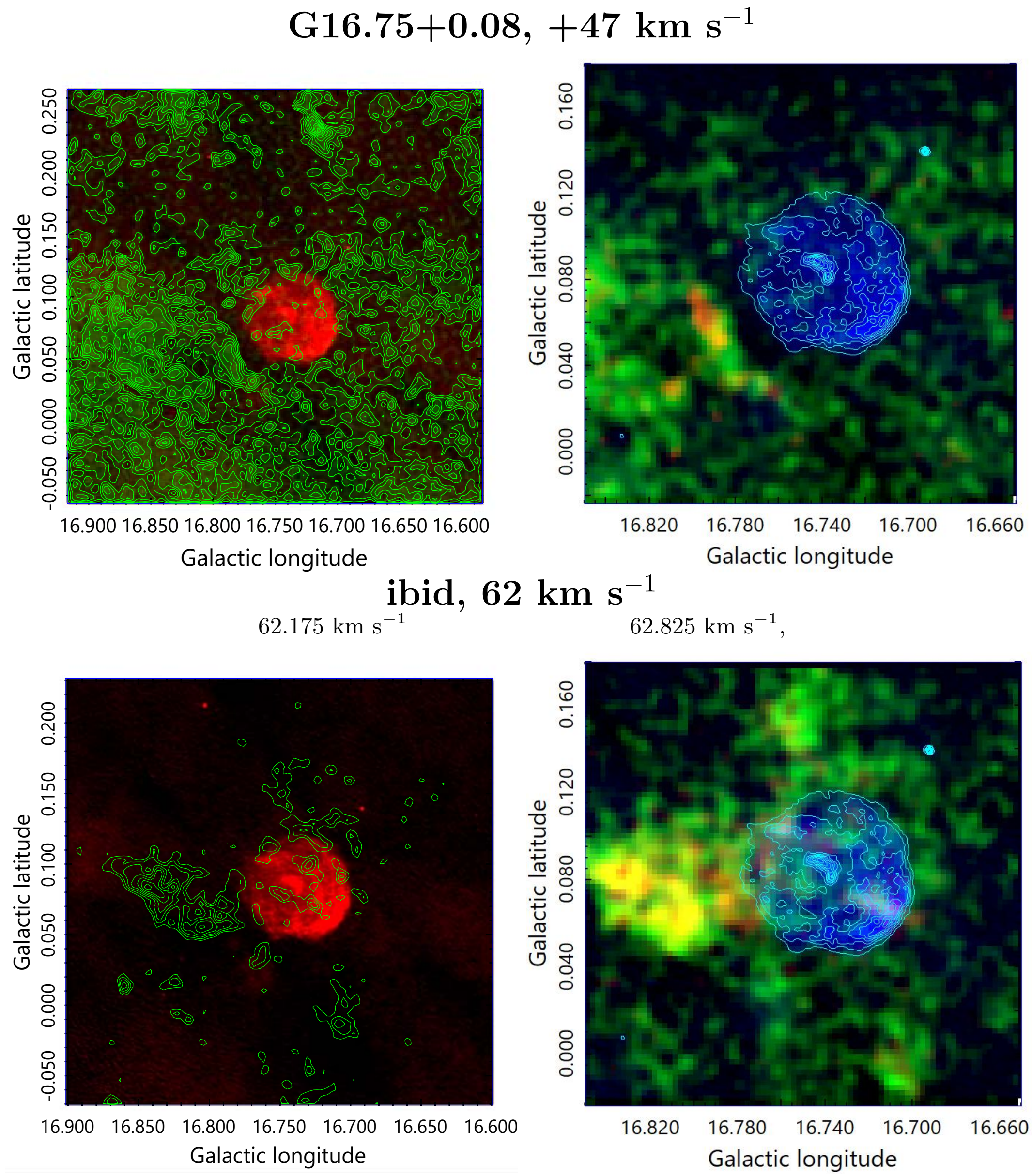

Figure 14. Same as figure 2, but for SNR G16.75+0.08, 47 km s^{-1}(^{12}CO from 2K by 1K; 20 cm from 0 by 4 mJy), or 62 km s^{-1}(4K, 1K; 0, 8mJy).

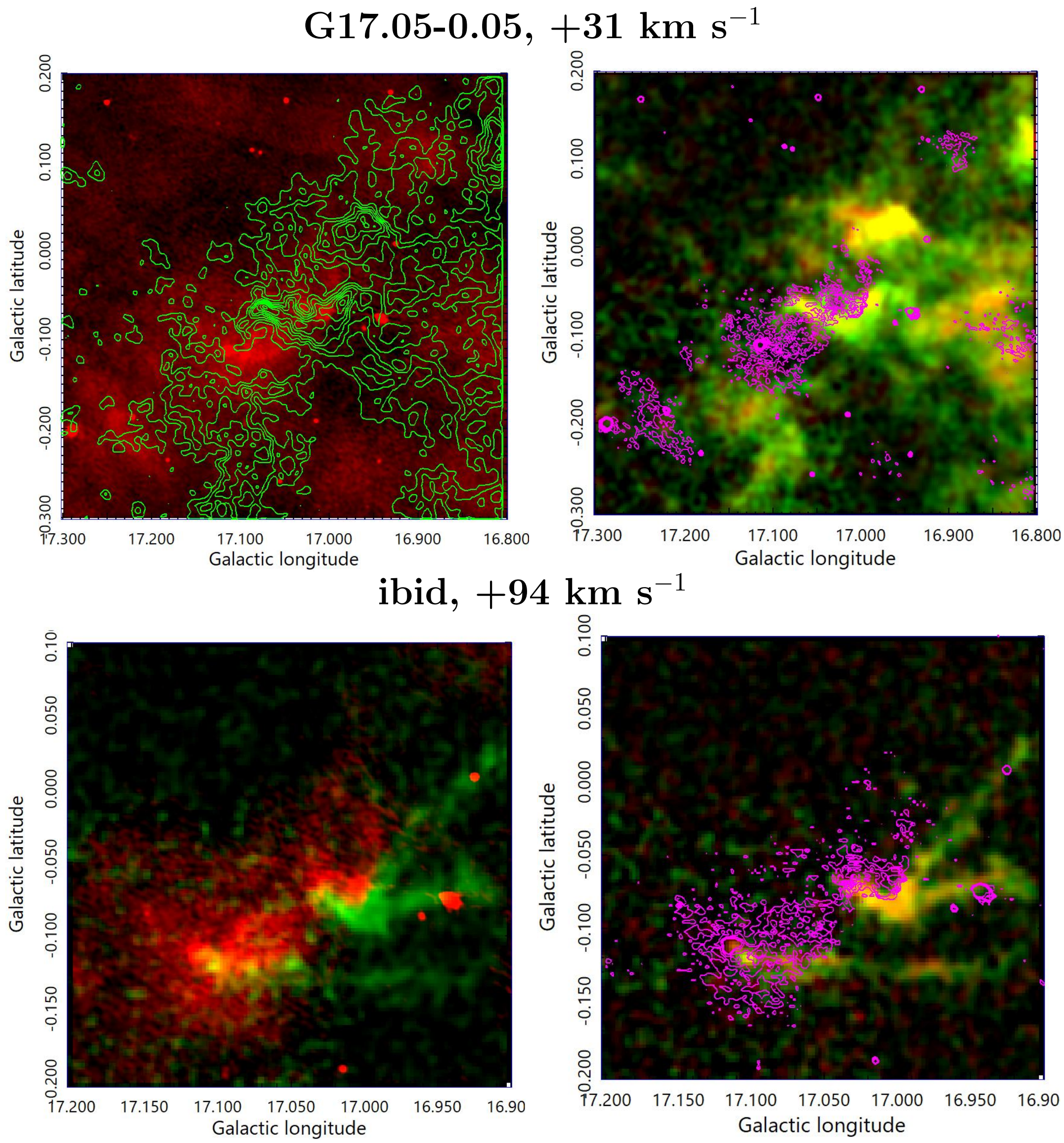

Figure 15. Same as figure 2, but for SNR G17.05-0.05, 94 km s^{-1}. (Top) 30.975 km s^{-1}, G(^{12}CO) on R(20 cm) auto; R(^{13}CO 0-5K) G(^{12}CO 0-15K) on 20-cm cont. (from 1 by 0.25mJy beam^{-1}). (Bottom) 94.025, G(^{12}CO) on R(20 cm) auto; 93.375 R(^{13}CO 0-5K), G(^{12}CO 0-15K), cont.(20 cm 1 by 0.25mJy beam^{-1})

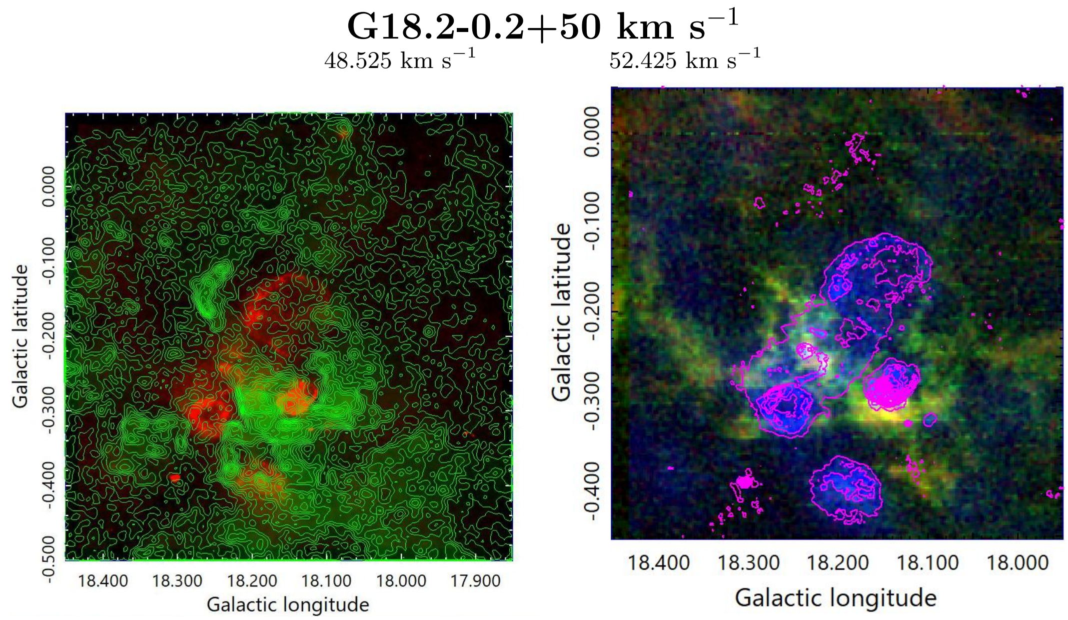

Figure 16. Same as figure 2, but for SNR G18.2-0.2, 48.525 km s^{-1}. ^{12}CO contours on 20 cm in red (0-2mJy beam^{-1}). R(^{13}CO 0 to 15 K) / G(^{12}CO 0 to 40 K)/contours (20 cm; start 2, step 1 mJy beam^{-1})

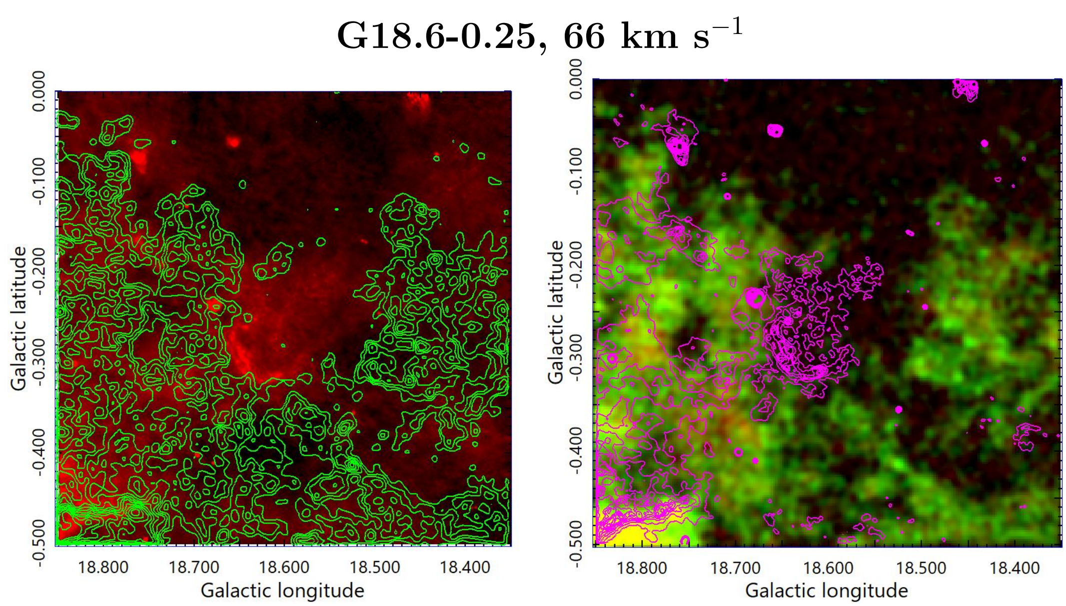

Figure 17. Same as figure 2, but for G18.6-0.25+66 km s^{-1}. ^{12}CO contours at 66.075 km s^{-1}on 20cm auto; R(^{13}CO 0 - 5 K) / G(^{12}CO 0 - 15 K) / contours (20 cm; start 1.5, step 4 mJy beam^{-1})

G18.8+0.35 +20, Kes 67

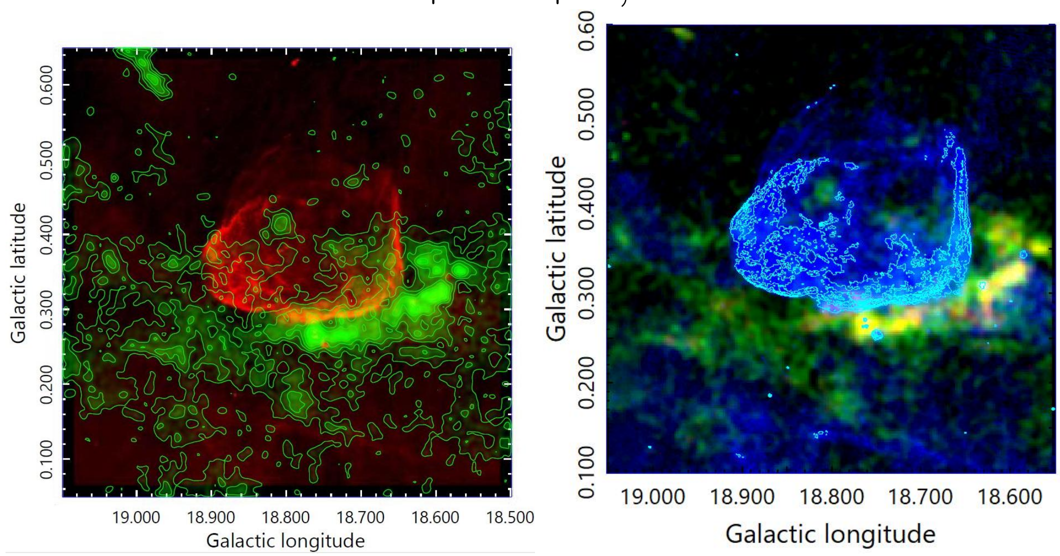

Figure 18. Same as figure 2, but for G18.8+0.35, +20 km s^{-1}superposed on 20 cm in red (auto). R (^{13}CO 1 - 5 K) / G(^{12}CO 1 - 12 K)/contours (20cm, start 2, step 2 mJy beam^{-1}).

G20.0-0.2+65 km s^{-1}

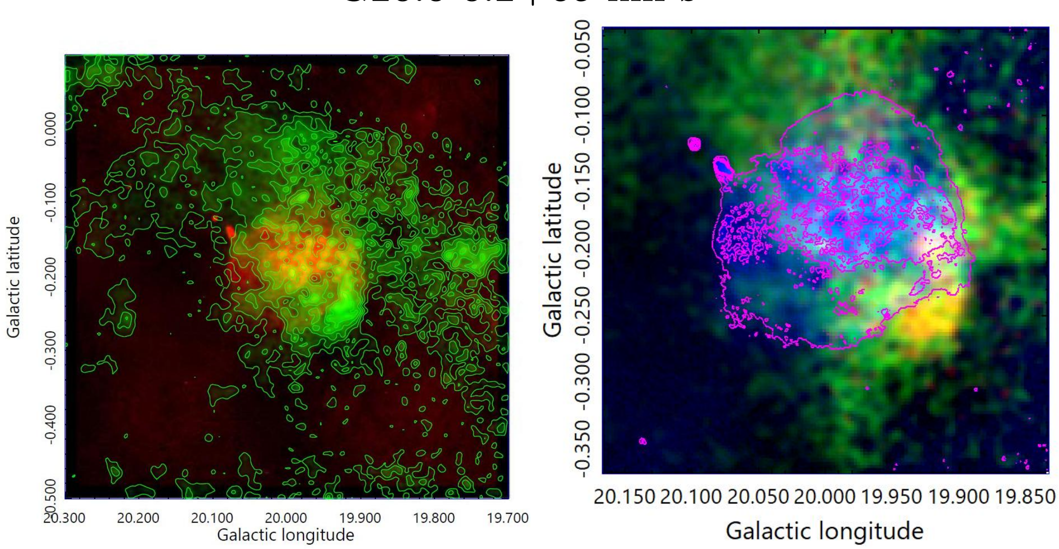

Figure 19. Same as figure 2, but for G20.0-0.2, 64.775 km s^{-1}: ^{12}CO on 20 cm (auto); R (^{13}CO 1 - 6 K) / G(^{12}CO 1 - 12 K) / contours (20 cm, start 1, step 1 mJy beam^{-1} .)

G21.8-0.5+83 km s^{-1}, Kes 69

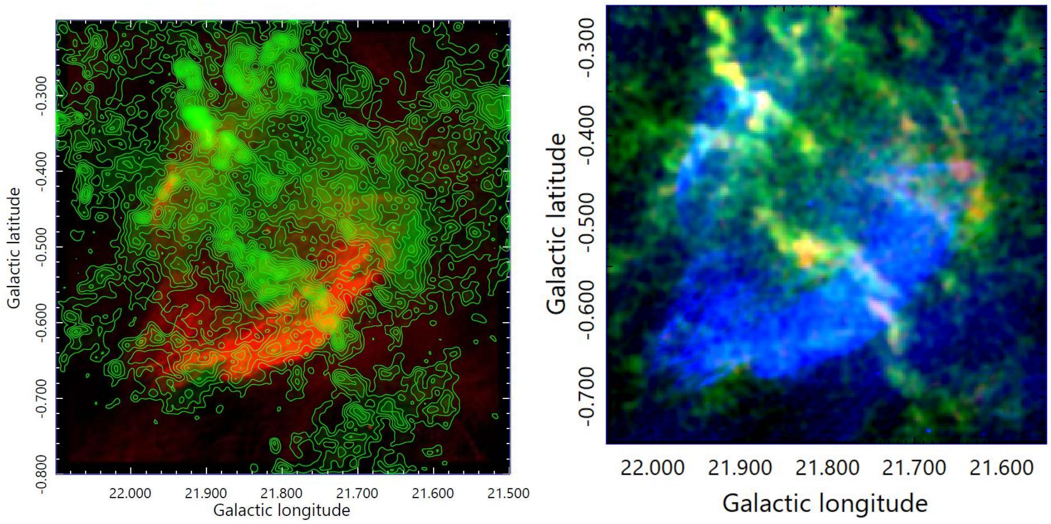

Figure 20. Same as figure 2, but for G21.18-05+82.975 km s^{-1} ^{12}CO contour start 4K, step 1K superposed on 20 cm in red. R(^{13}CO , 1 to 4 K) / G(^{12}CO , 1 to 12 K) / 20 cm (0 to 3 mJy beam^{-1}).

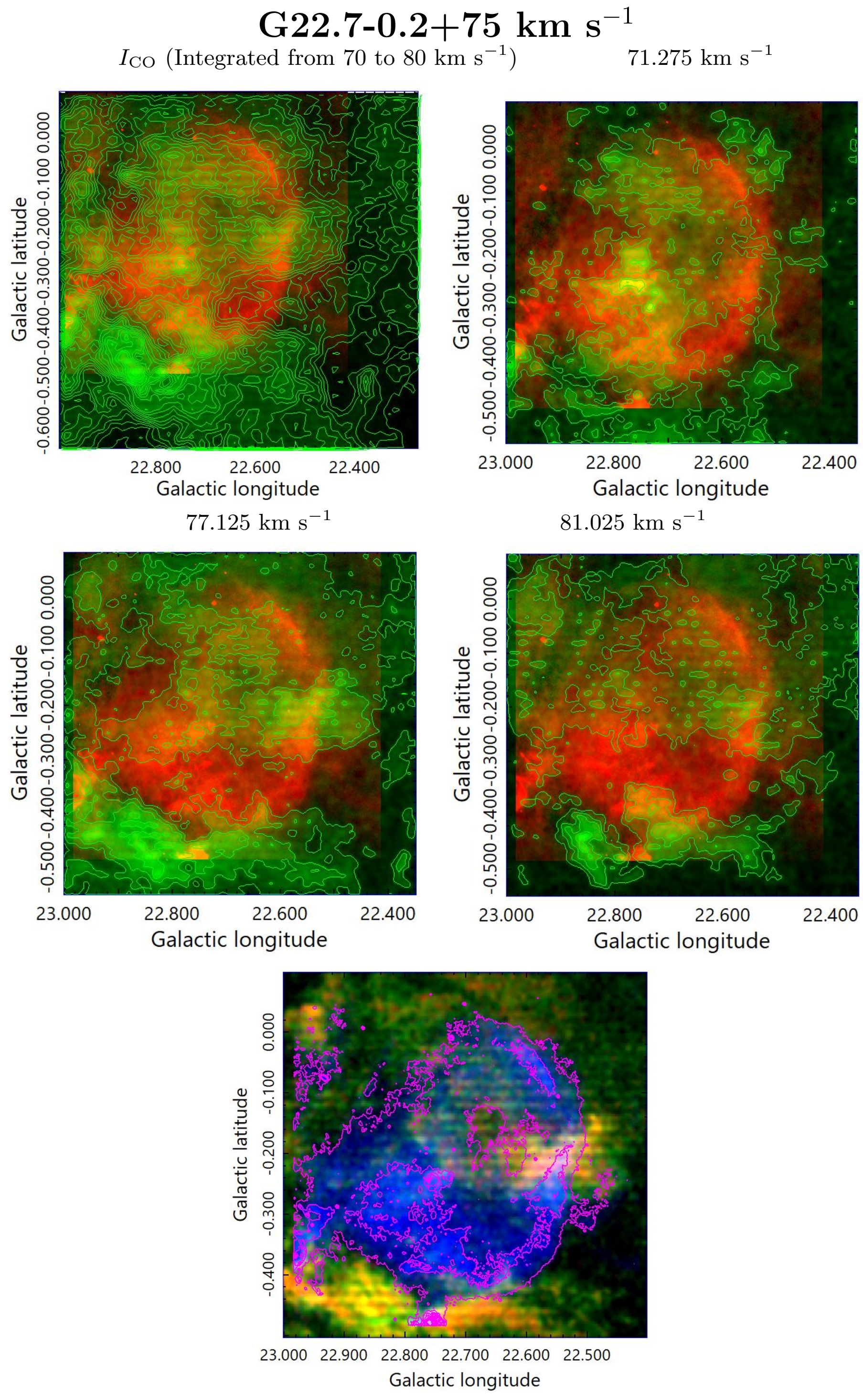

Figure 21. Same as figure 2, but for G22.27-0.2+75 km s^{-1}. (Top left) $I_{\rm CO}$ intergarted from 70 to 80 km s^{-1}, contours start 25, step 25 K km s^{-1}; (Top right and middle) ^{12}CO $T_{\rm B}$ at different velocities, contours start 4, step 2 K. (Bottom) 77.125 km s^{-1}, R(^{13}CO 1 - 6 K) / G(^{12}CO 1 - 20 K) / contours (20 cm; start 1.5, step2 mJy beam^{-1}).

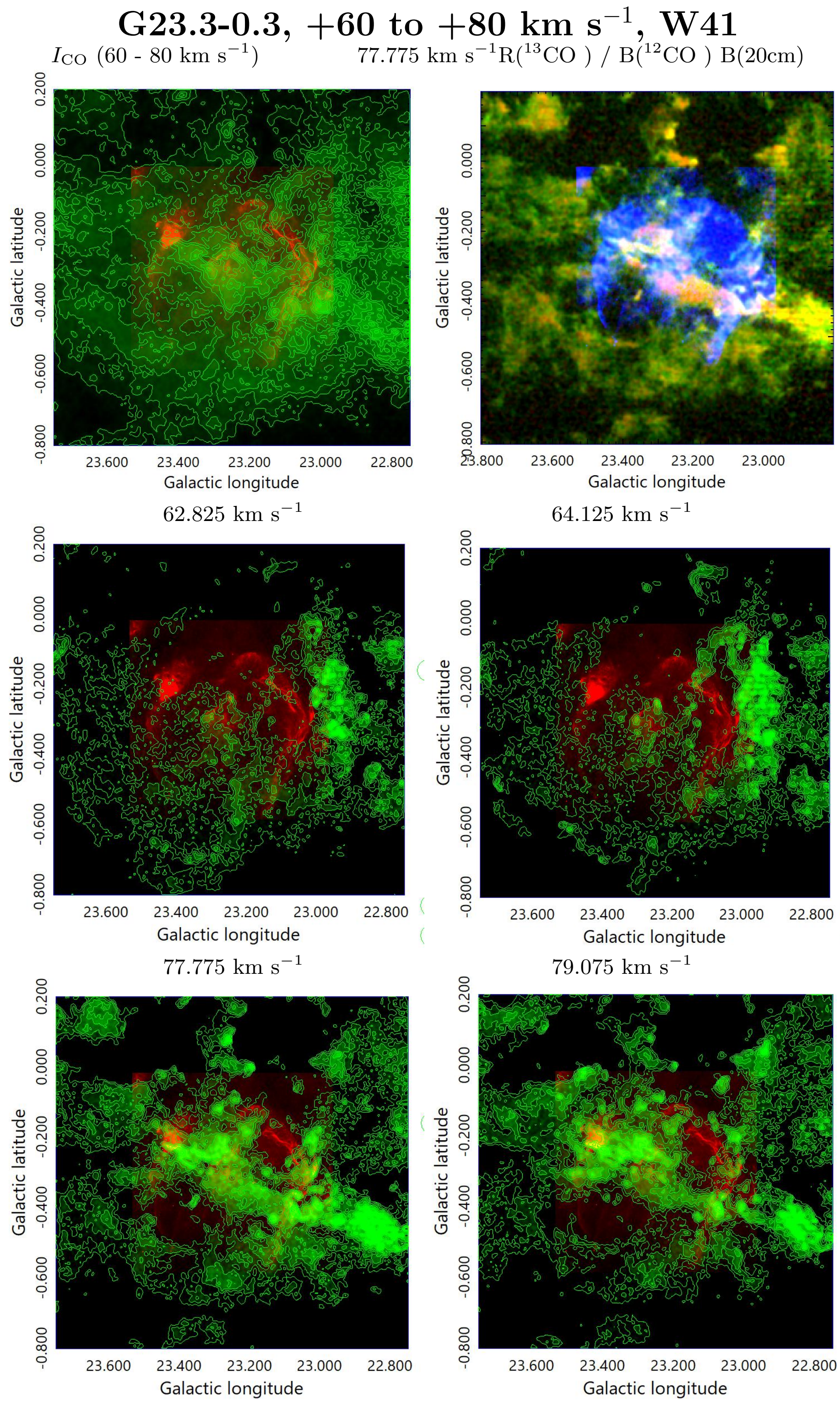

Figure 22. Same as figure 2, but for G23.3-0.3+7775 W41. (Top left) I_{CO} contours every 25 K km s^{-1}. (Top right) 77.775 km s^{-1}, R(^{13}CO 0-5K) B(^{12}CO 0-15K) B(20cm 1-2mJy beam^{-1}). Channel maps contours start 4K, step 1K, and 20-cm in red from 0 to 8 mJy beam^{-1} .

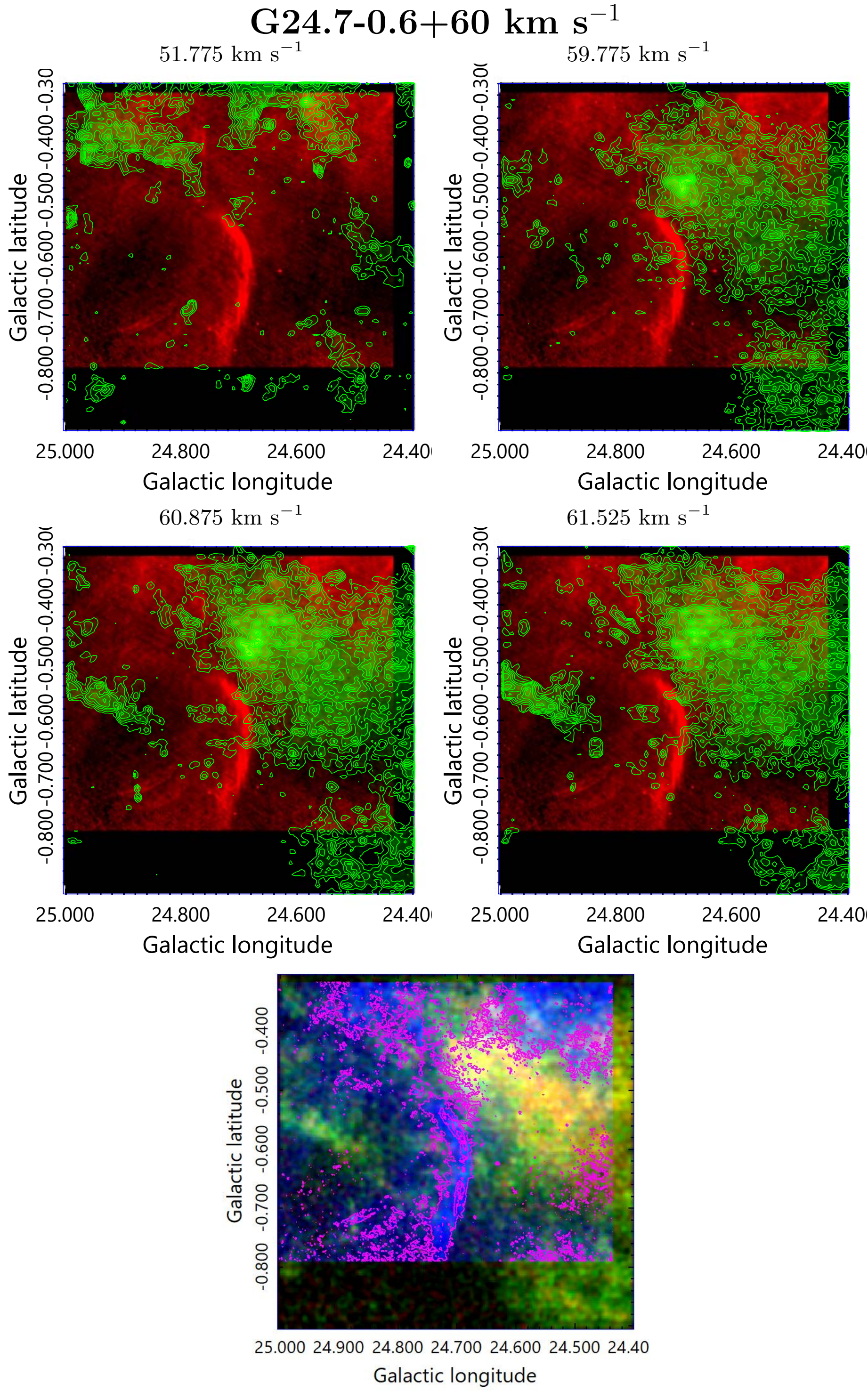

Figure 23. G24.7-0.6+60 km s^{-1}; ^{12}CO (start 4K, step 1K) on 20 cm (red from 0 to 2 mJy beam^{-1}). R(^{13}CO , 0, 5 K) / G(^{12}CO , 0, 15 K) / 20 cm (1, 1 mJy beam^{-1} .

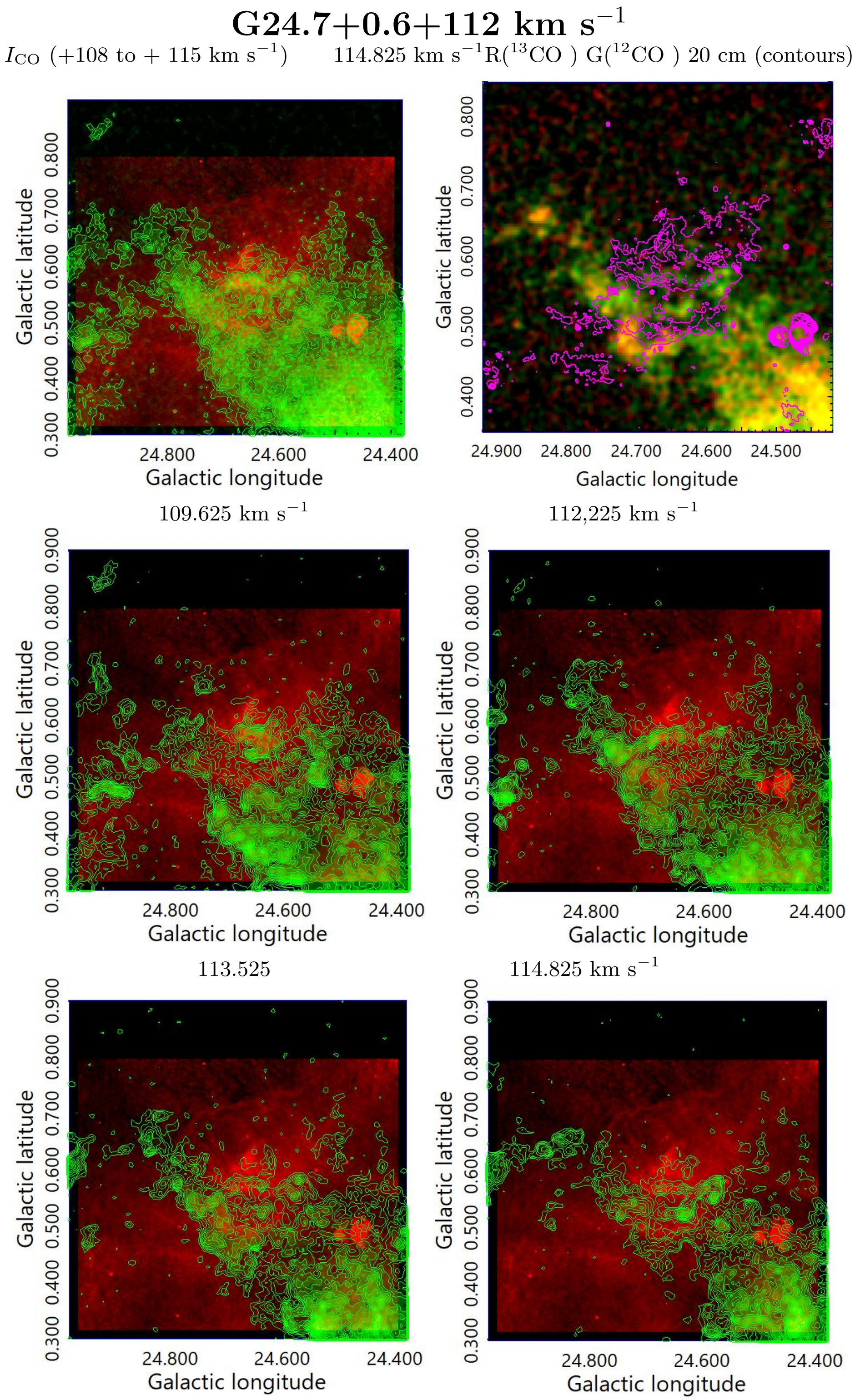

Figure 24. G24.7+0.6+112 km s^{-1}. $I_{\rm CO}$ (108 to 115 km s^{-1}) on 20 cm (red, auto). R (^{13}CO , 0 to 3 K) / G(^{12}CO , 0 to 12 K) / contours (20 cm, start 1.5, step 0.5 mJy beam^{-1}). ^{12}CO (contours, start 2 K, step 1 K) on 20 cm (red from 0 to 3 mJy beam^{-1}).

G27.4+0.0+101 km s^{-1}, 4C-04.71

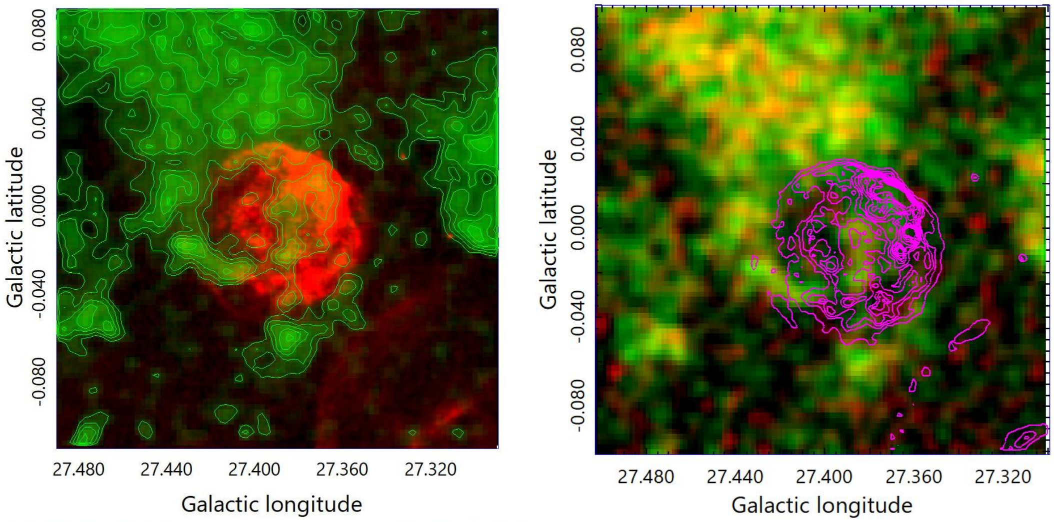

Figure 25. Same as figure 2, but for G27.4, 101.175 km s^{-1}on 20 cm continuum in red (auto). R(^{13}CO , 0 to 3K) G(^{12}CO , 0 to 10 K) on 20 cm (contours, start 2, step 1 mJy beam^{-1}).

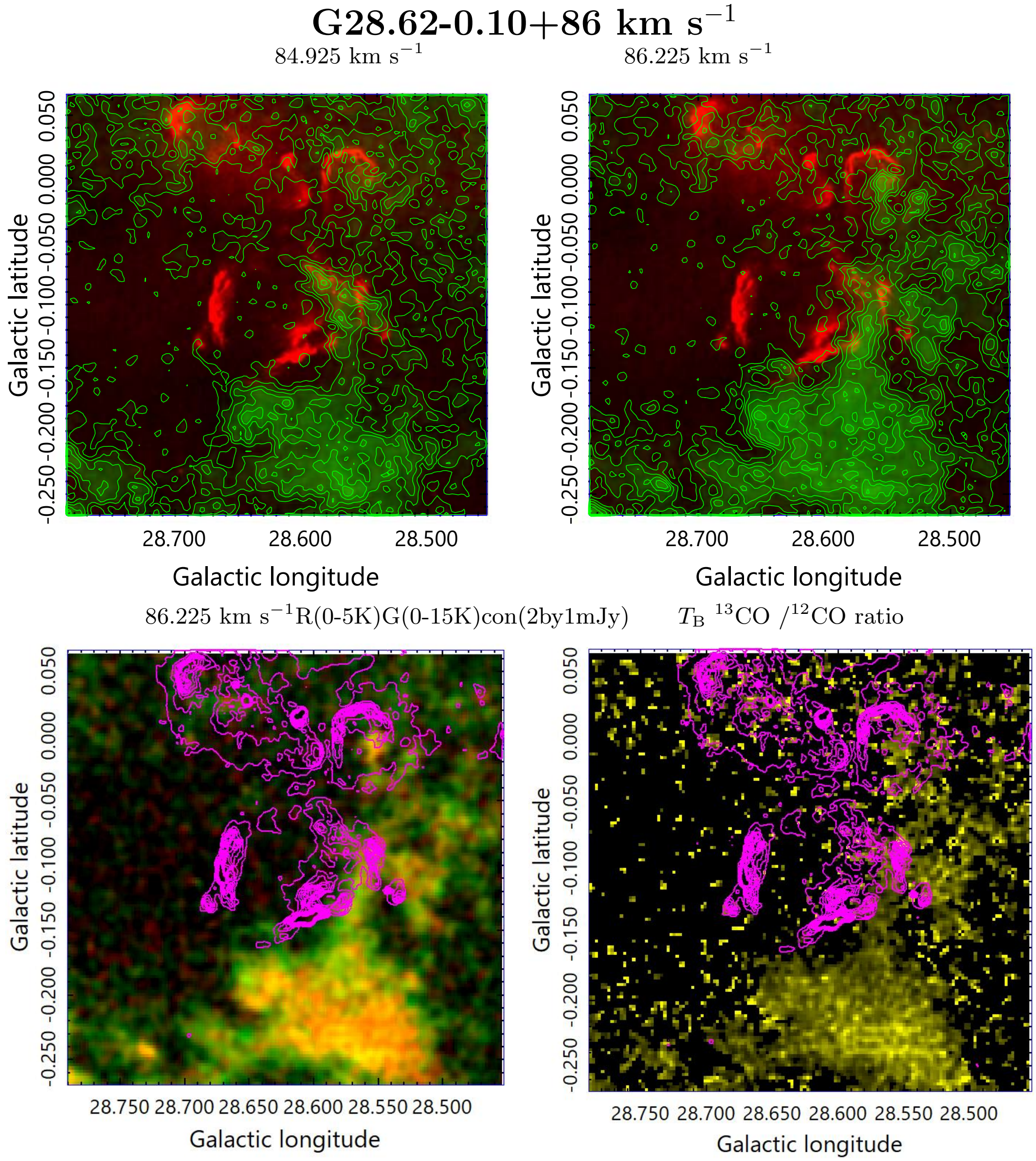

Figure 26. Same as figure 2, but for G28.62-0.10, +86 km s^{-1}. (Top) ^{12}CO contours (start 2, step 2 K) at 84.9 and 86.2 km s^{-1}superposed on 20-cm continuum (red, 0 to 8 mJy beam^{-1}). (Bottom left) R(^{13}CO , 0 to 5 K) G(^{12}CO , 0 to 15 K) on 20 cm (contours start 2, step 1 mJy beam^{-1}). (Bottom right) ^{13}CO /^{12}CO $T_{\rm B}$ ratio by yellow scale superposed on the 20-cm continuum contours.

G28.62-0.10 and N49 (G28.83-0.25) at 86.225 km s^{-1}

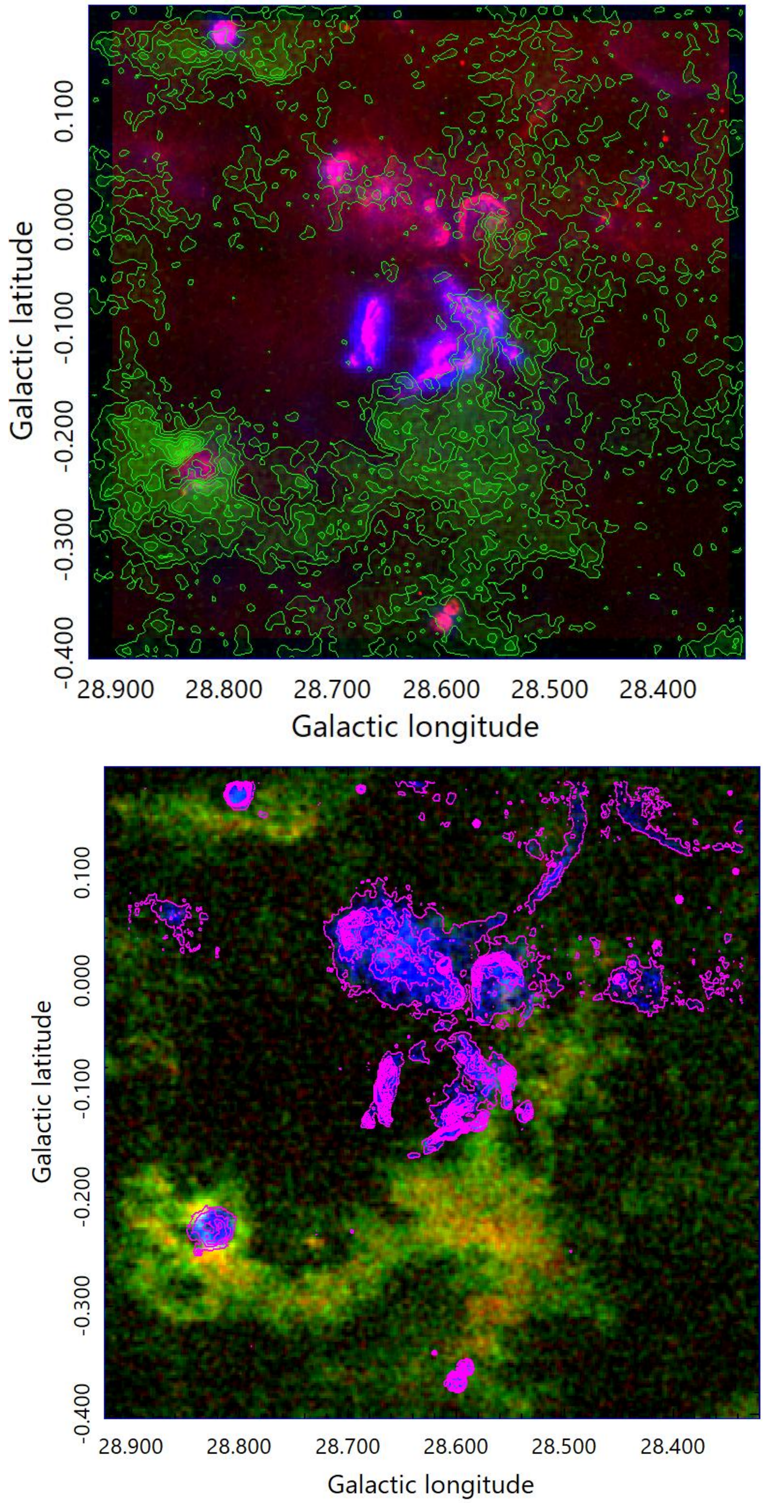

Figure 27. Same as figure C, but ^{12}CO $T_{\rm B}$ at 86.2 km s^{-1}for wider area including Spitzer Bubble N49 (G28.83-0.25) (Deharveng et al. 2010), showing evidence for the co-existence of the SNR and star forming region, both being embedded in the same molecular cloud.

G29.6+0.1, 99.2 km s^{-1}

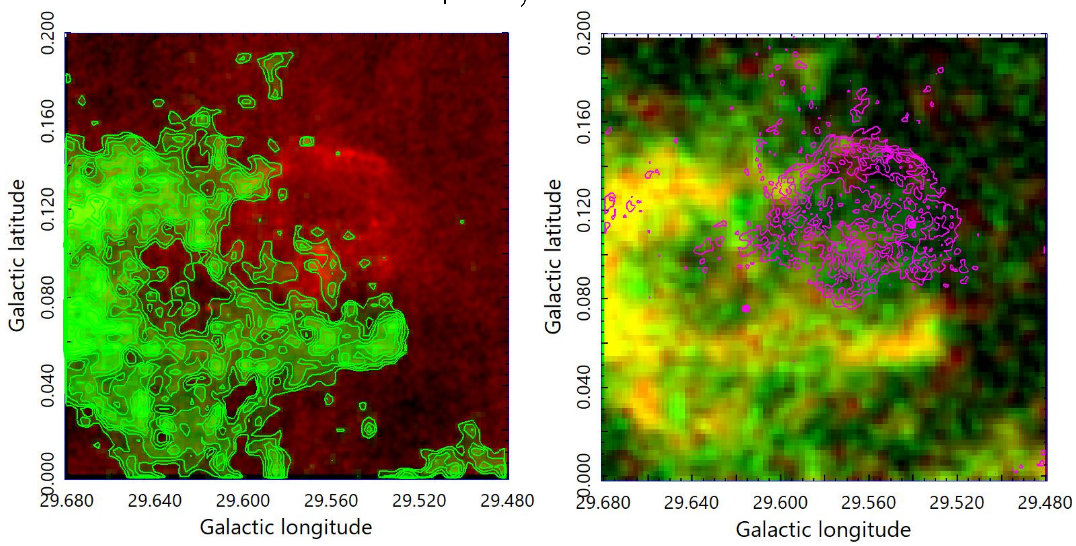

Figure 28. Same as figure 2, but for G29.6+0.1, 99.2 km s^{-1}. (Left) ^{12}CO contours (start 6 K, step 1 K) superposed on 20 cm (red). (Right) R(^{13}CO , 0 to 3 K) / G(^{12}CO , 0 to 12 K) / contours (20 cm, start 1, step 0.2 mJy beam^{-1})

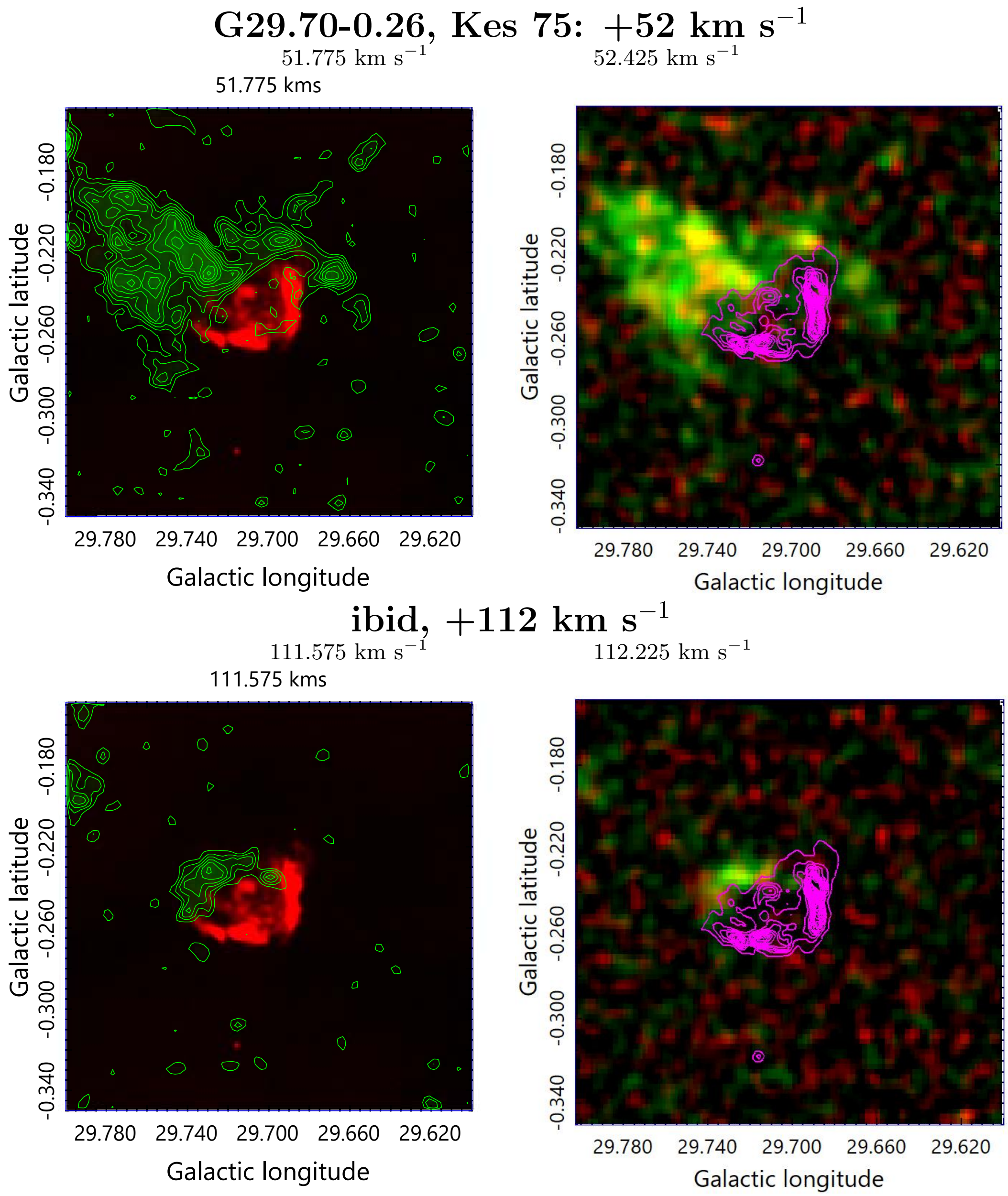

Figure 29. Same as figure 2, but for G29.70-0.26 Kes 75: 51.775 km s^{-1}or 111.575 km s^{-1}. (Top left) ^{12}CO contours (start 2 K, step 1 K) at +51.775 km s^{-1}superposed on 20-cm (red; 0 to 10 mJy beam^{-1}). (Top right) R(^{13}CO 0 to 3 K) / G(^{12}CO 0 to 10 K) / 20cm (contours, start 2, step 5 mJy beam^{-1}). (Bottom) Same, but at 112 km s^{-1}.

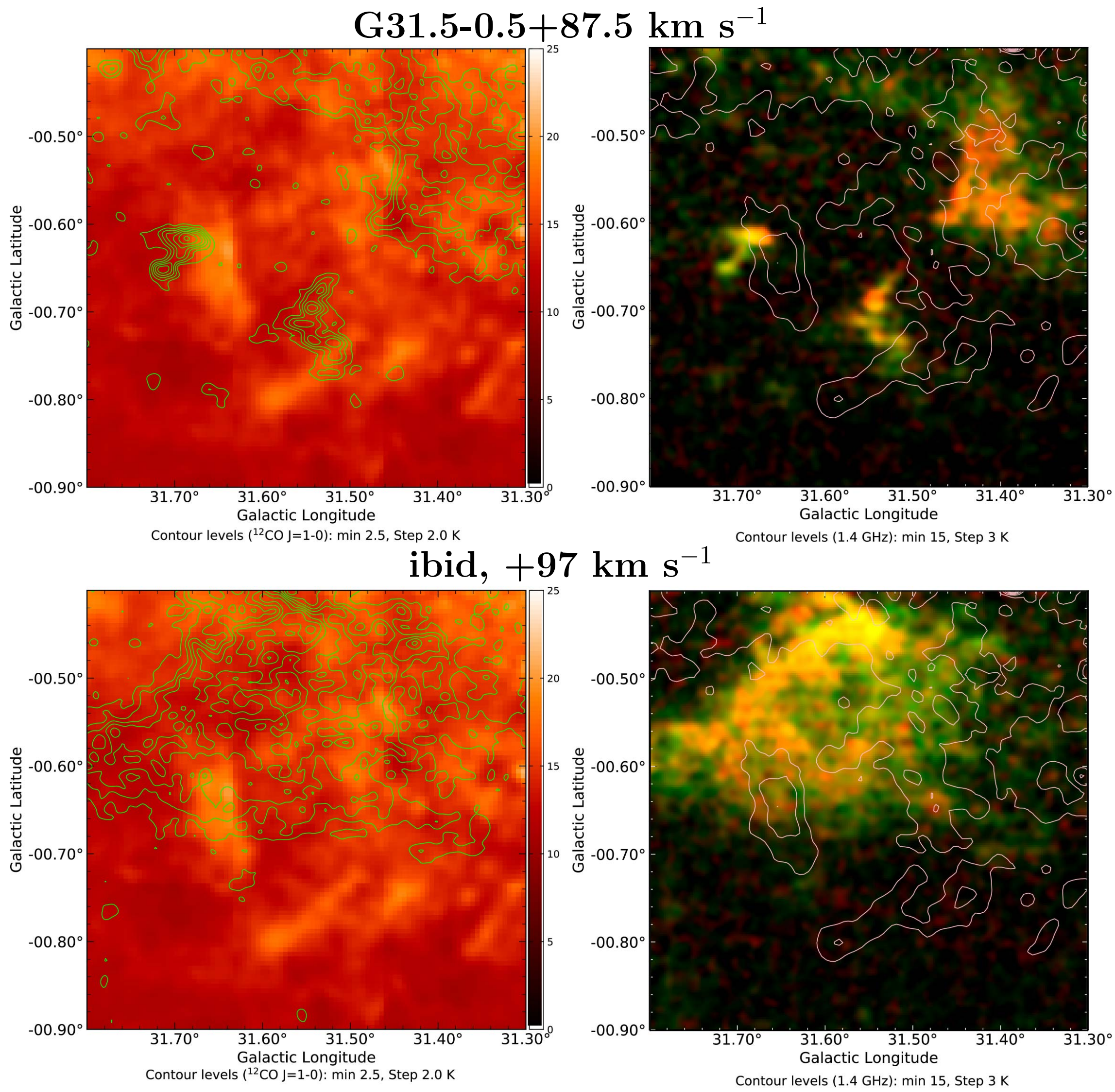

Figure 30. Same as figure 2, but for G31.5-0.5 at +87.5 km s^{-1}(top): (Left) ^{12}CO contours superposed on the radio continuum map in red. (Right) Radio continuum contours superposed on the two color composite image, red and green showing ^{12}CO and ^{13}CO $J=$1-0 respectively. Note: From hereon, the intensity scales are indicated at the bottom of each figure. (Bottom) Same, but at +97 km s^{-1}.

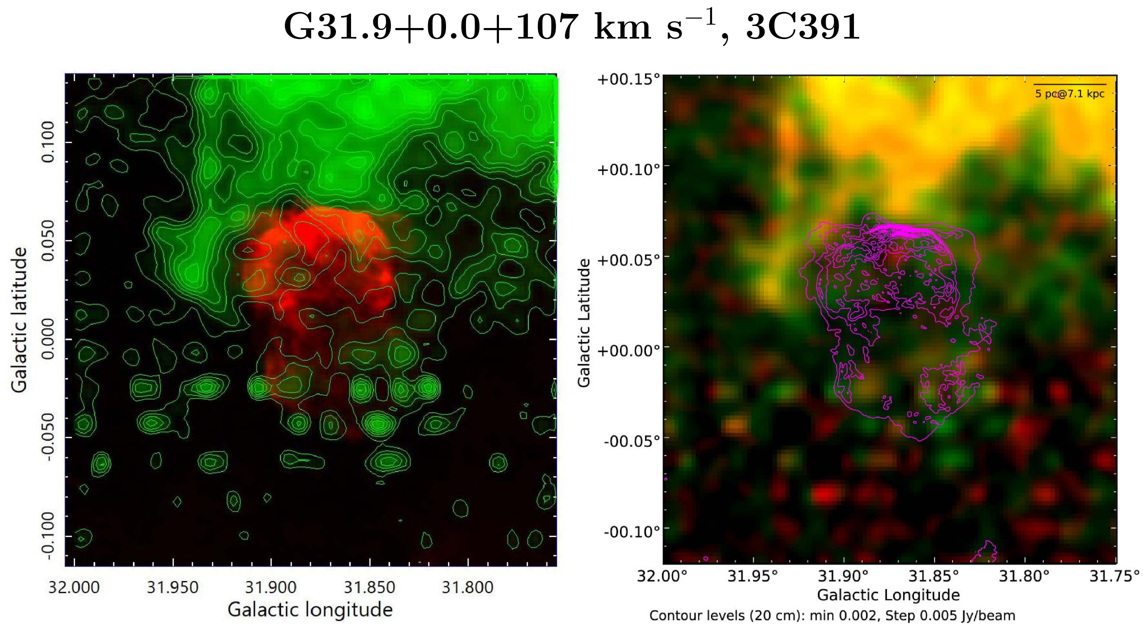

Figure 31. Same as figure 30, but for SNR G31.9+00, 107.025 km s^{-1}.

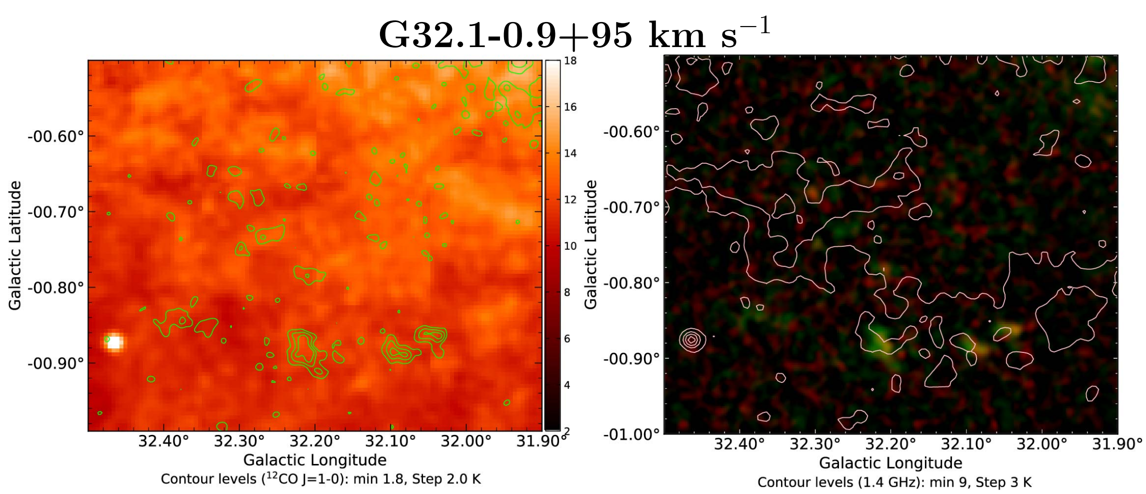

Figure 32. Same as figure 30, but for SNR G32.1-0.9+97 km s^{-1}.

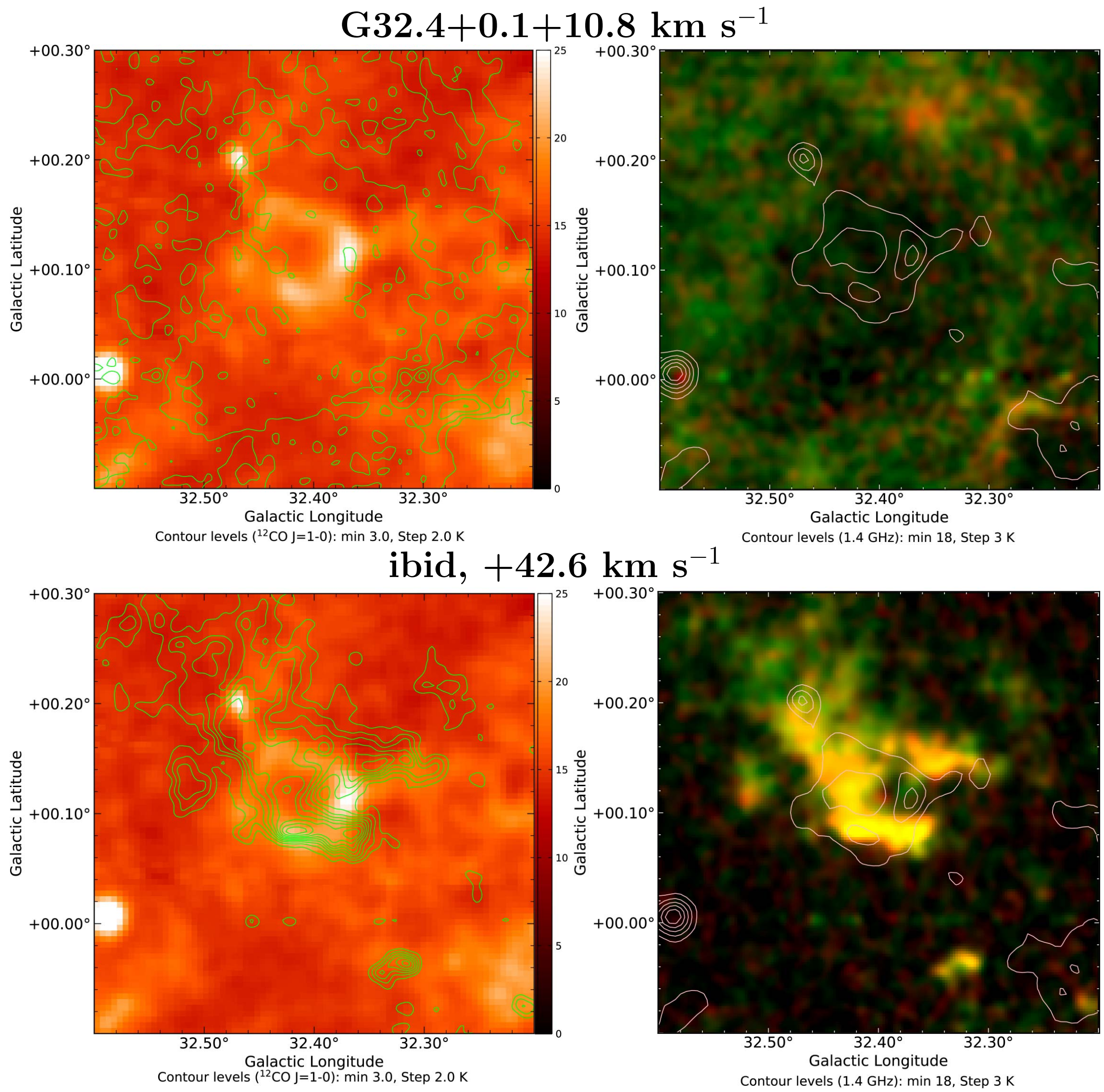

Figure 33. Same as figure 30, but for SNR G32.4+0.1 at +10.8 km s^{-1}(top), or at +42.6 km s^{-1}(bottom)

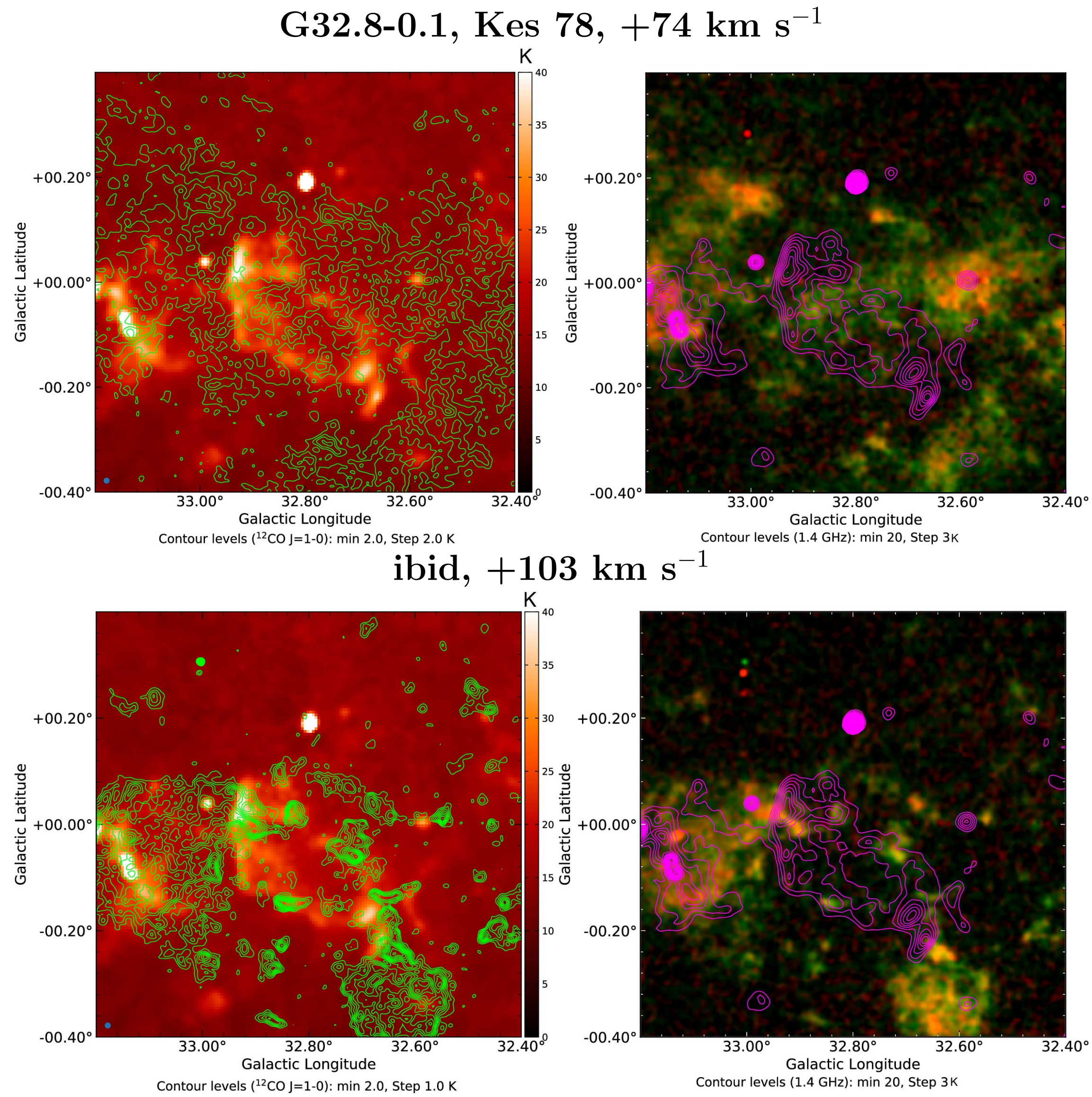

Figure 34. Same as figure 30, but for SNR G32.8-0.1 (Kes 78) at +74 km s^{-1}(top) or at +103 km s^{-1}(bottom).

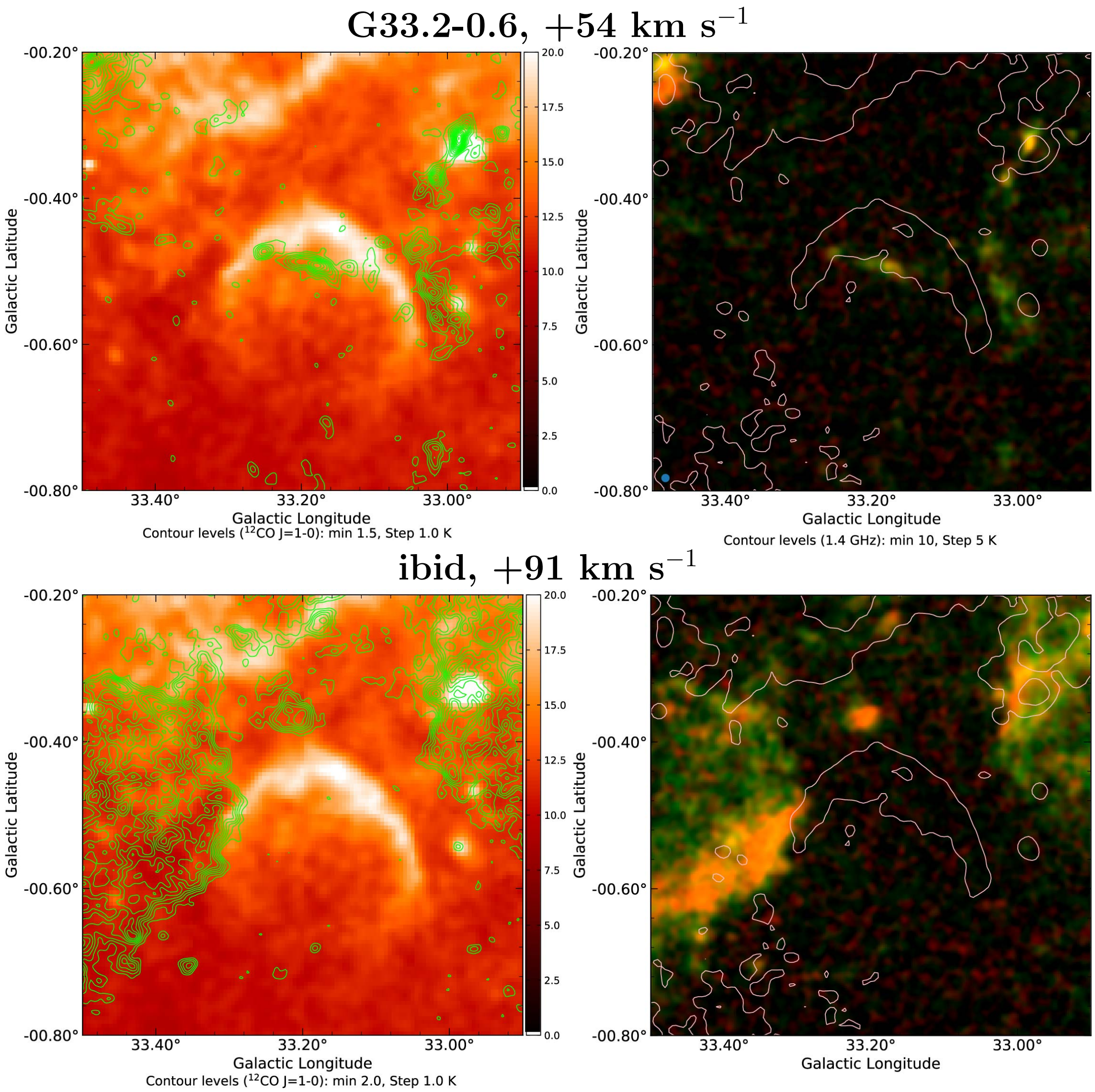

Figure 35. Same as figure 30, but for SNR G33.2-0.6 at +54 km s^{-1}(top) or at +91 km s^{-1}(bottom).

G33.7+0.05+70 km s^{-1}, Kes 79, 4C00.70, HC13

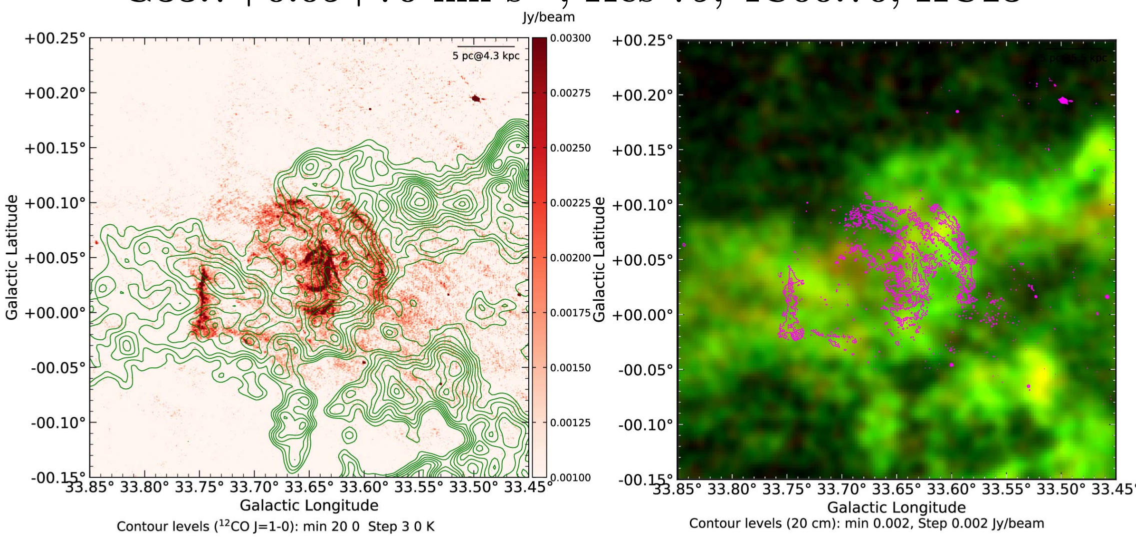

Figure 36. Same as figure 30, but for SNR G33.7+0.05+70 km s^{-1}.

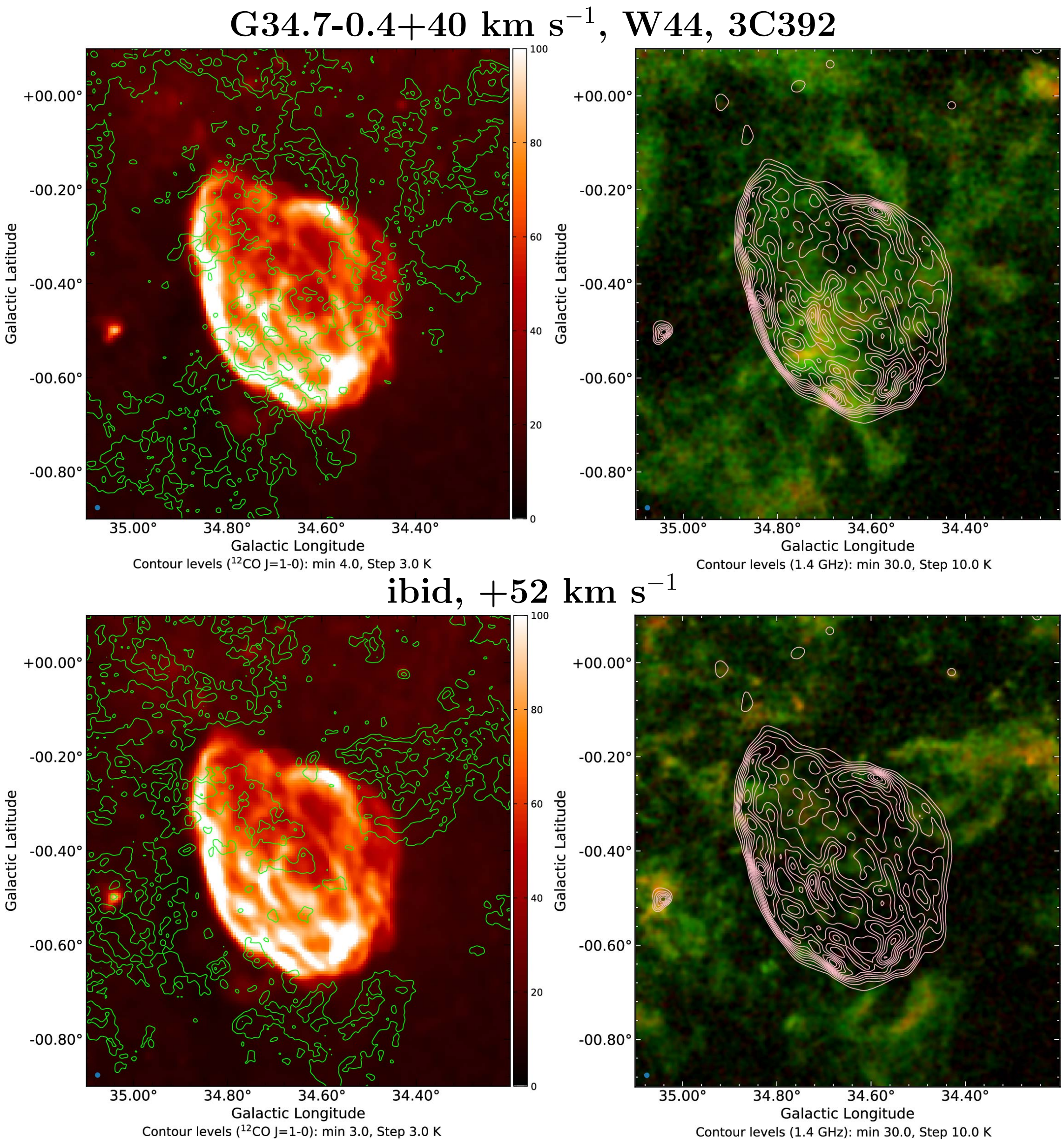

Figure 37. Same as figure 30, but for SNR G34.7-0.4+40 km s^{-1}, and +62 km s^{-1}.

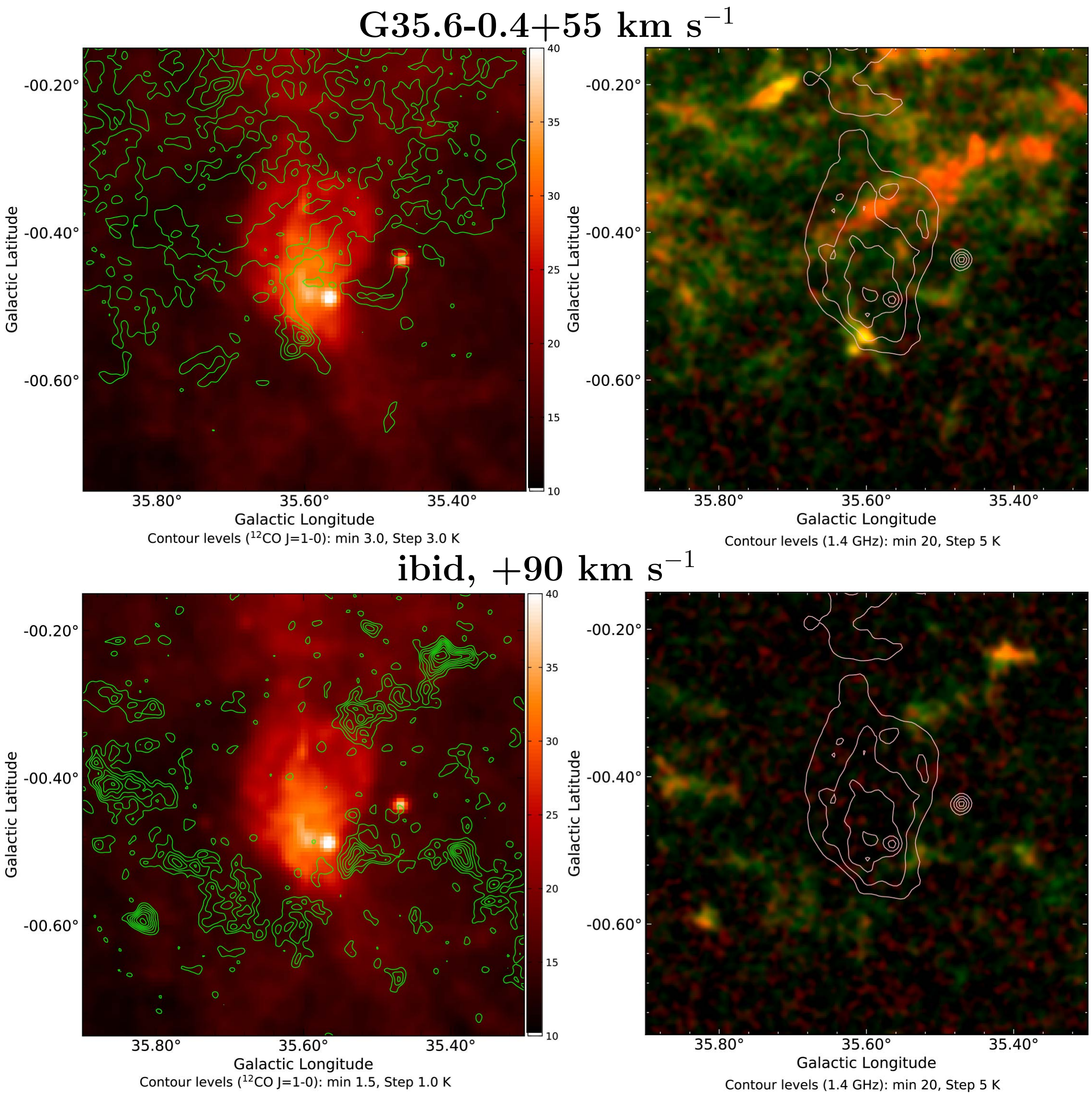

Figure 38. Same as figure 30, but for SNR G35.6-0.4, +55 and +90 km s^{-1}.

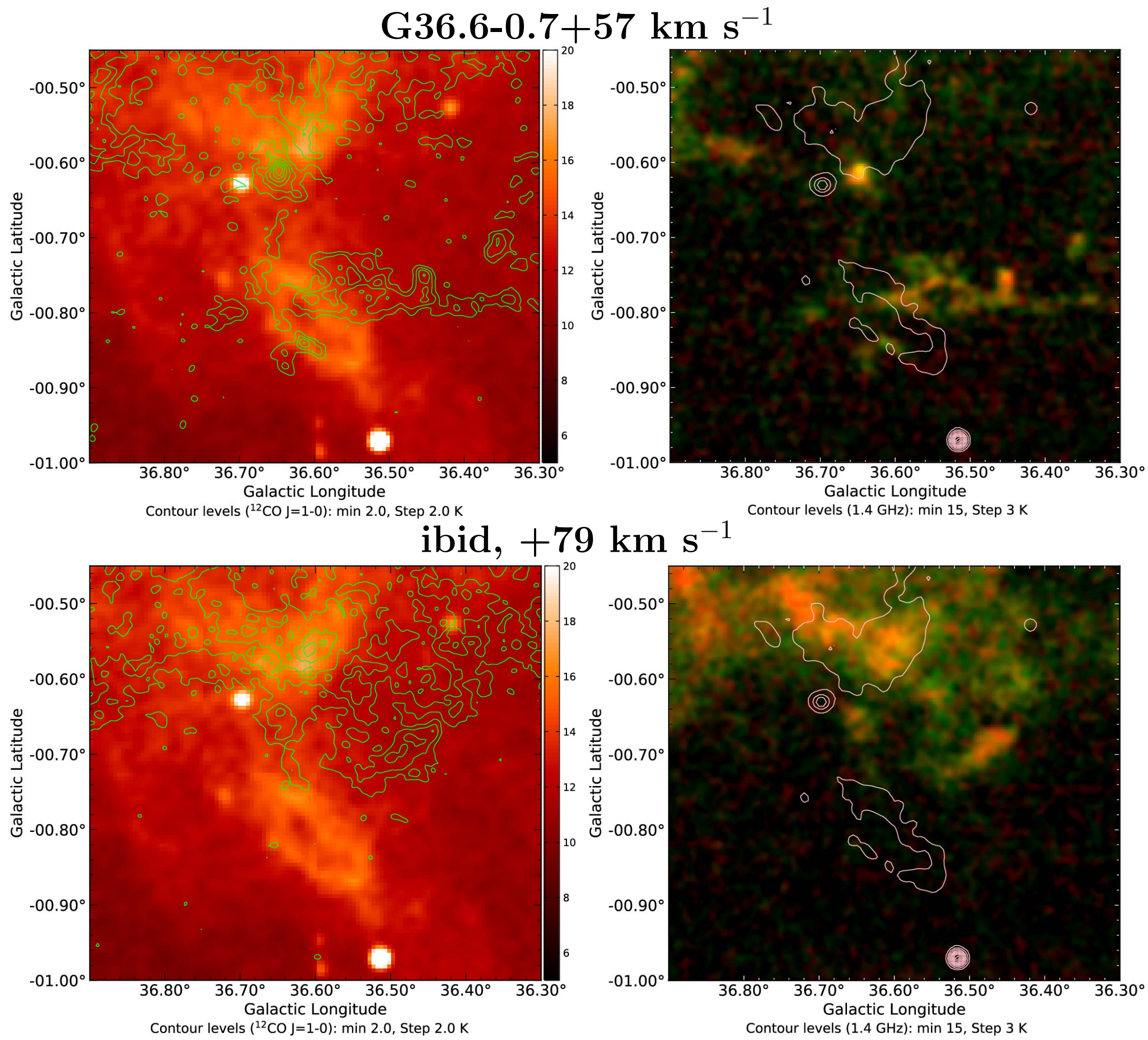

Figure 39. Same as figure 30, but for SNR G36.6-0.7 at +57 (top) or at +79 km s^{-1}(bottom).

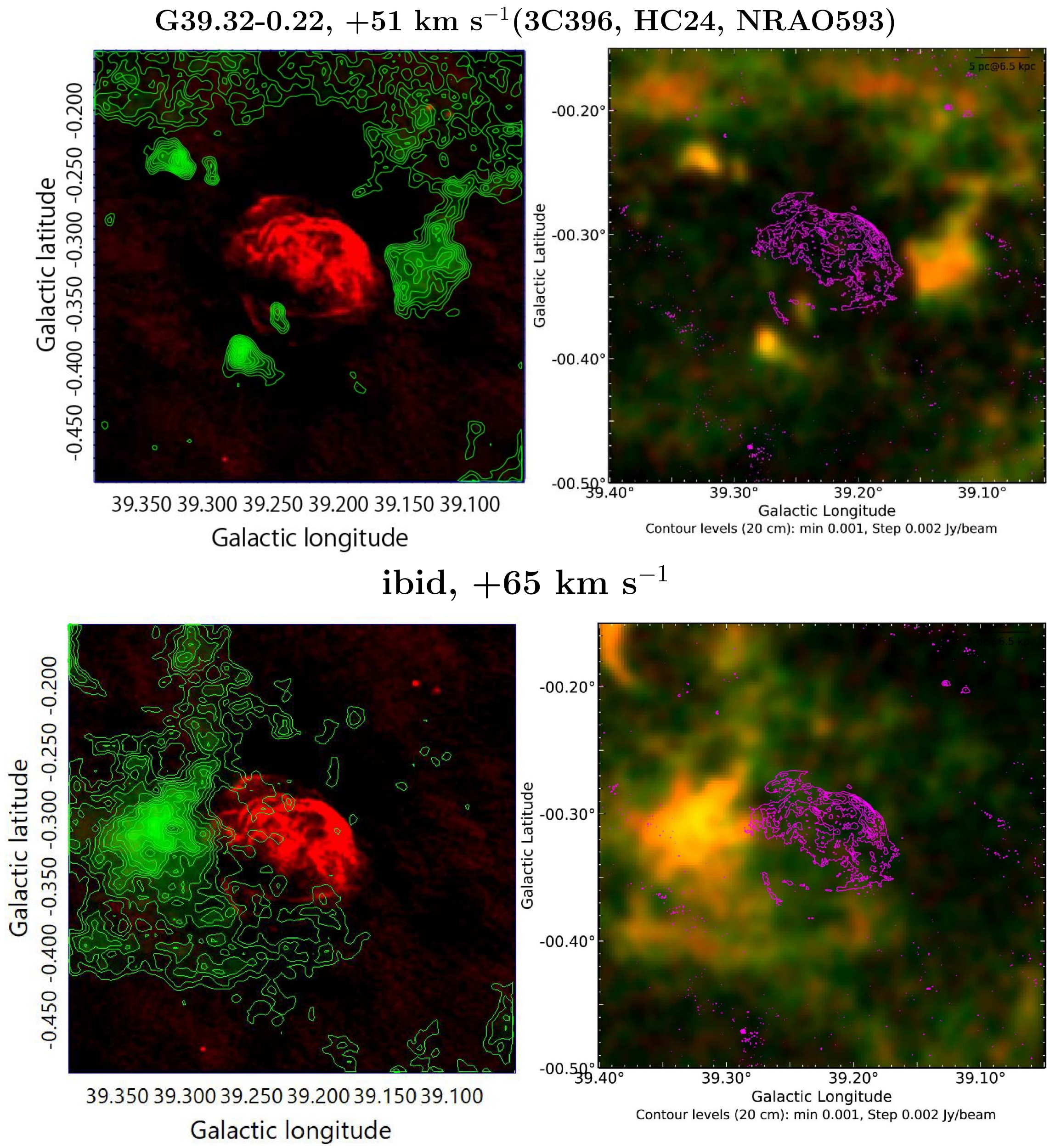

Figure 40. Same as figure 30, but for SNR G39.2-0.3, at two possible velocities, +51 or +65 km s^{-1}.

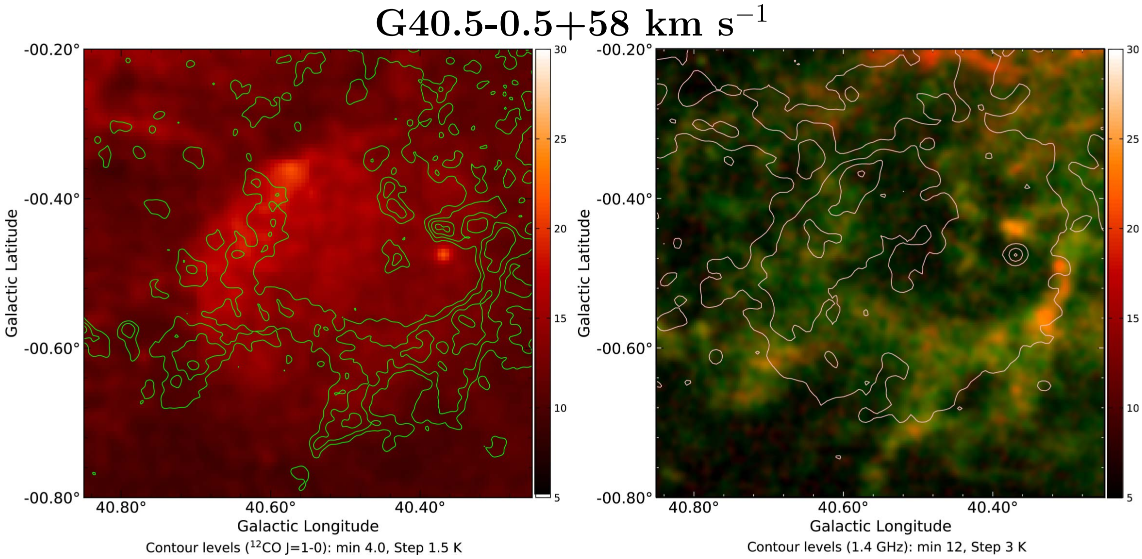

Figure 41. Same as figure 30, but for SNR G40.5-0.5+58 km s^{-1}.

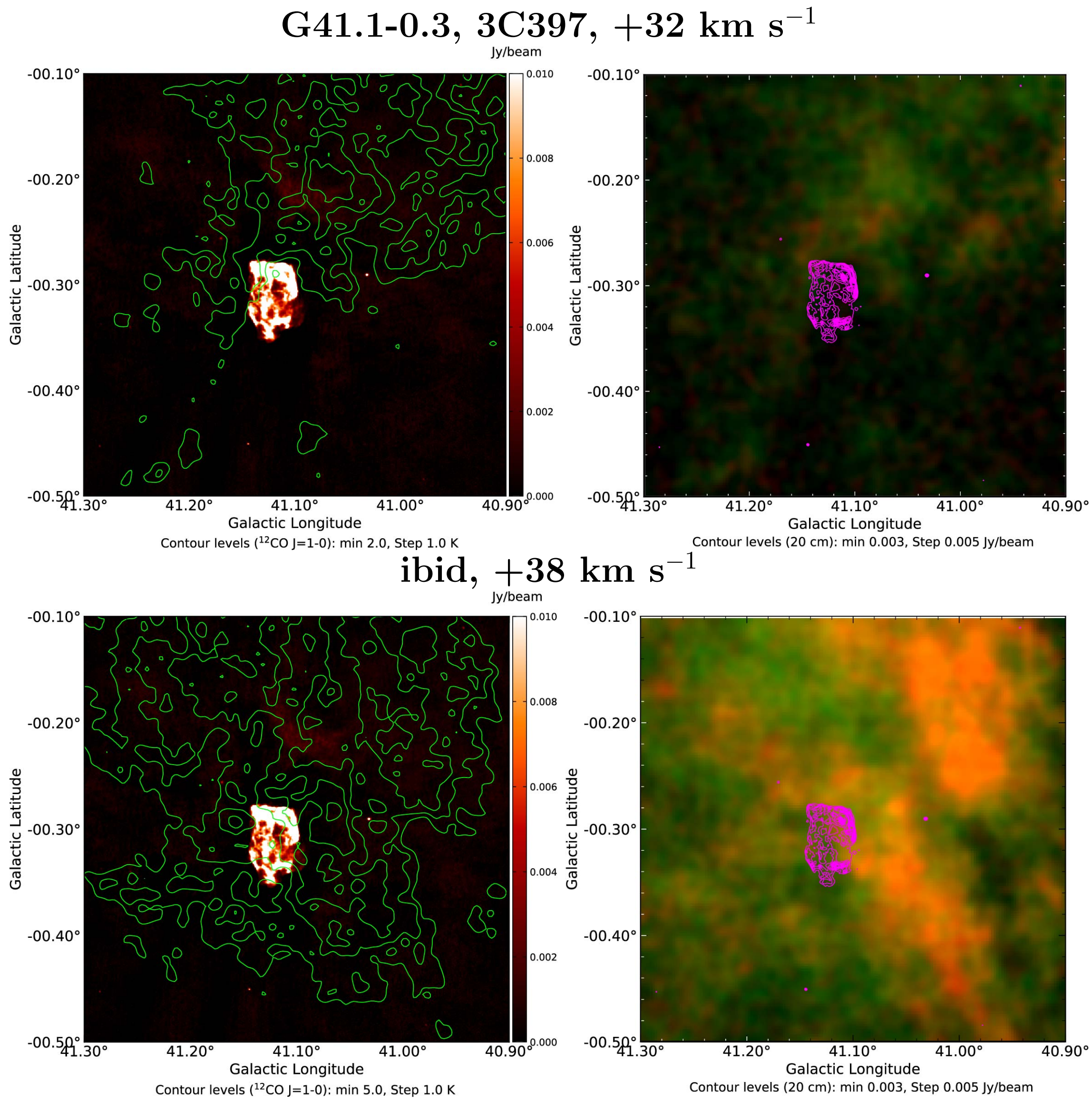

Figure 42. Same as figure 30, but for SNR G41.1-0.3, 3C 397, at +32 and +38 km s^{-1}.

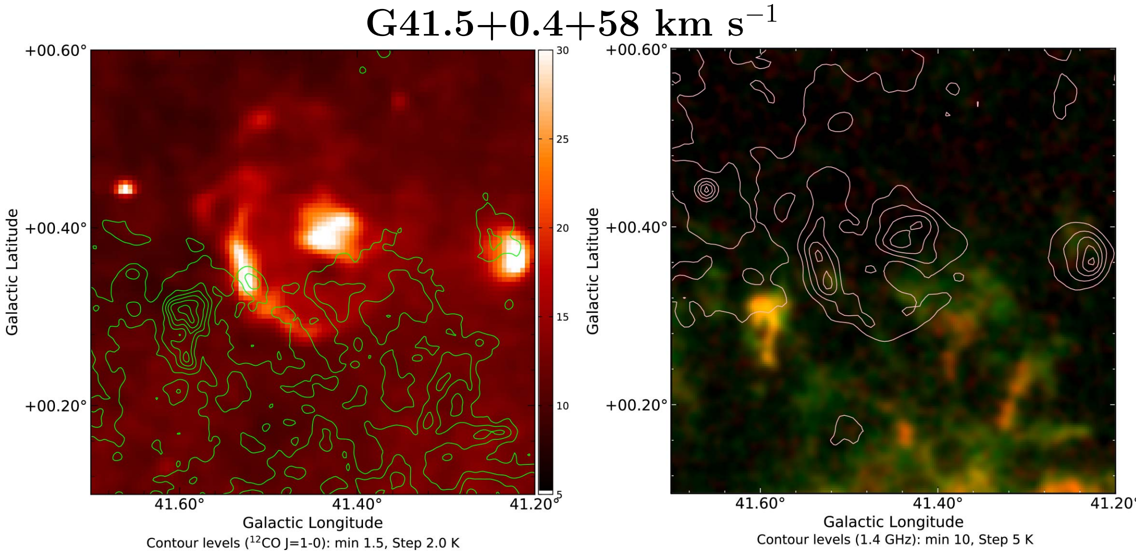

Figure 43. Same as figure 30, but for SNR G41.5+0.4+58 km s^{-1}.

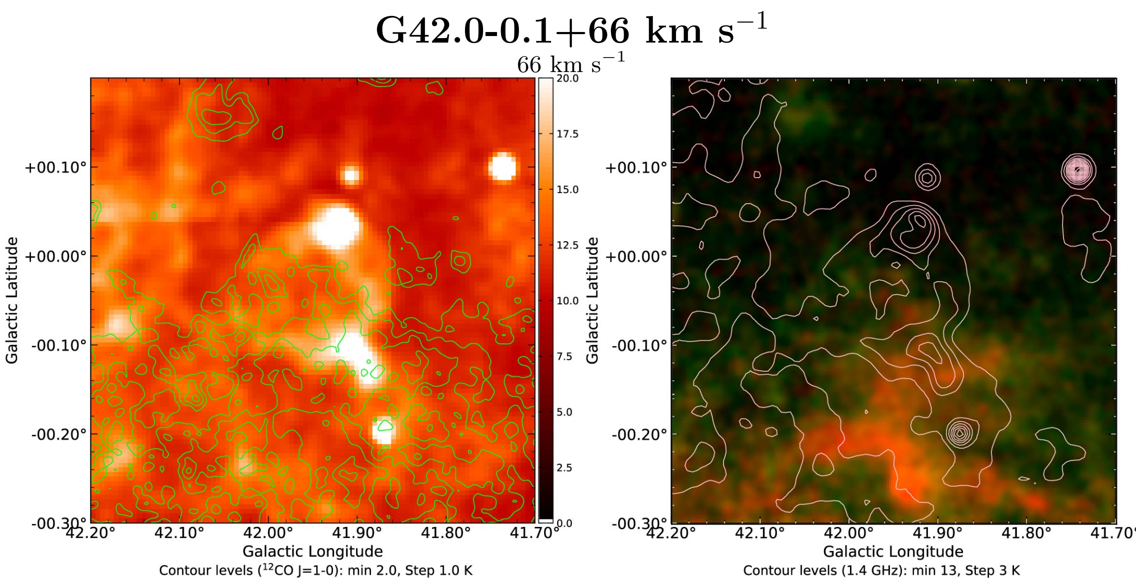

Figure 44. Same as figure 30, but for SNR G42.0-0.1+66 km s^{-1}.

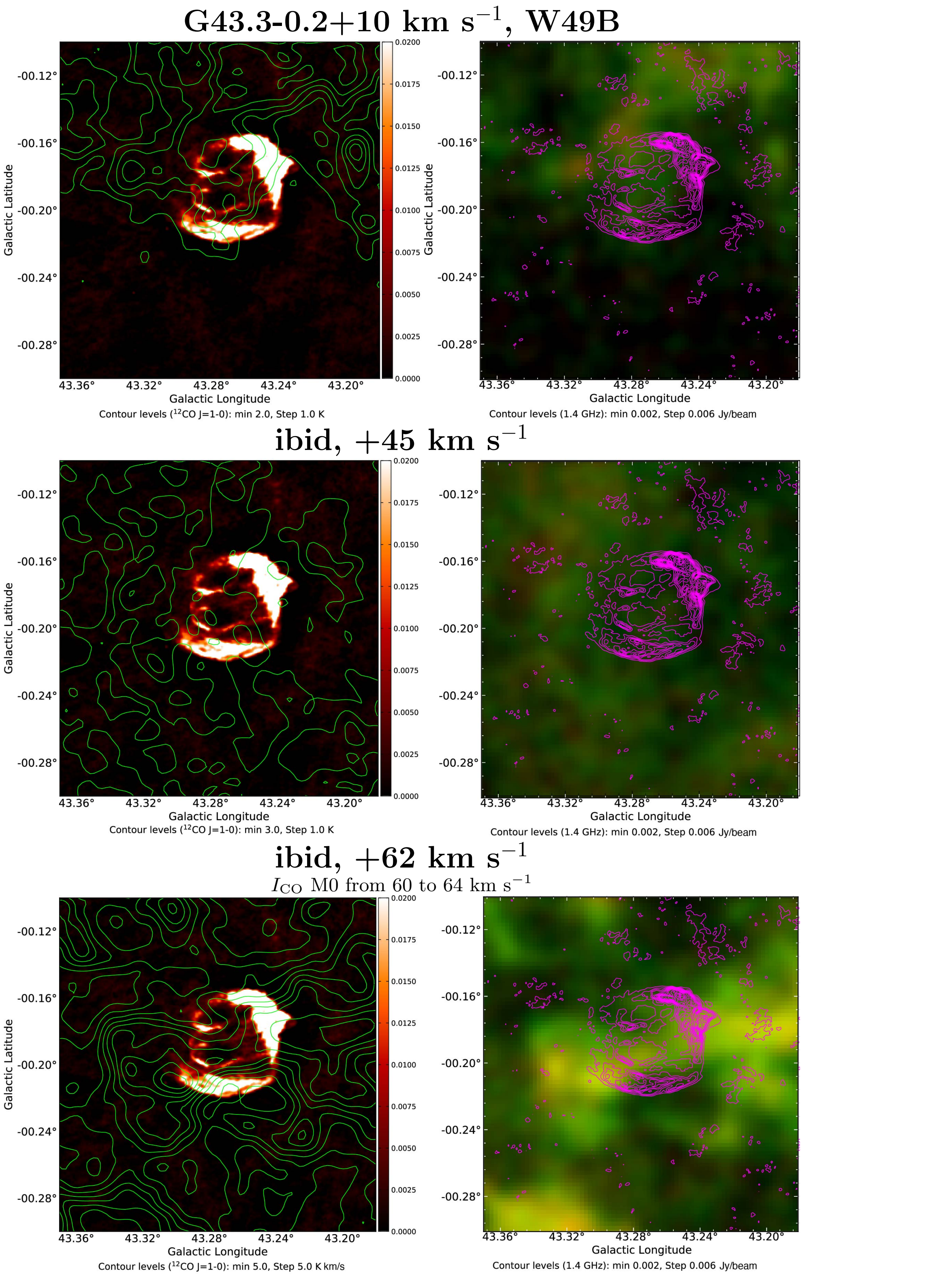

Figure 45. Same as figure 30, but for SNR G43.3-0.2+45 km s^{-1}, W49B at 10 km s^{-1}(top), 45 km s^{-1}(middle) or at 62 km s^{-1}(bottom).

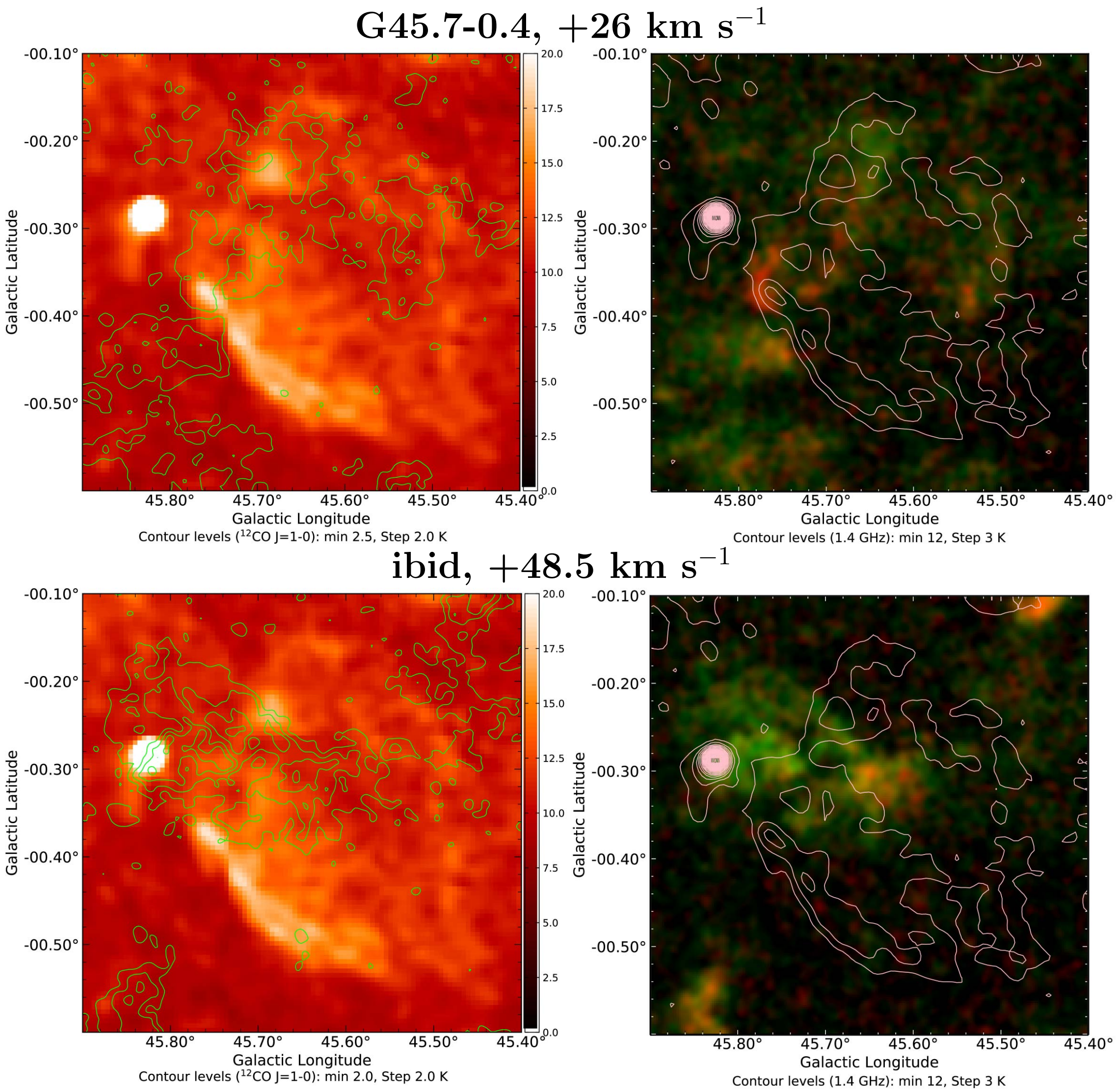

Figure 46. Same as figure 30, but for SNR G45.7-0.4 at +26 km s^{-1}(top), or at 48.5 km s^{-1}(bottom).

G46.8-0.3+52 km s^{-1}, HC30

$I_{\rm CO}$ M0 from 48 to 56 km s^{-1}

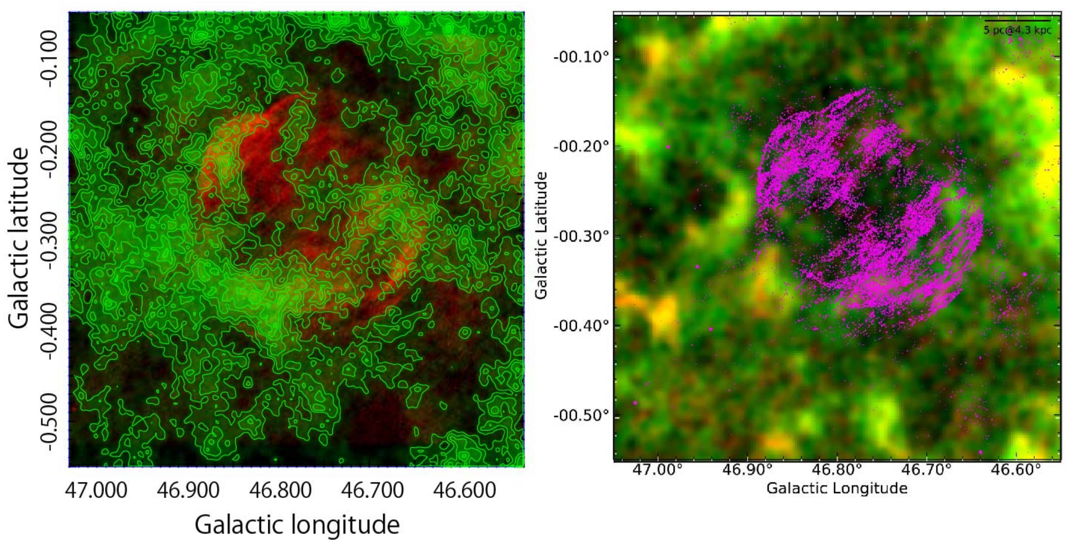

Figure 47. Same as figure 30, but for SNR G46.8-0.3; 52 km s^{-1}.

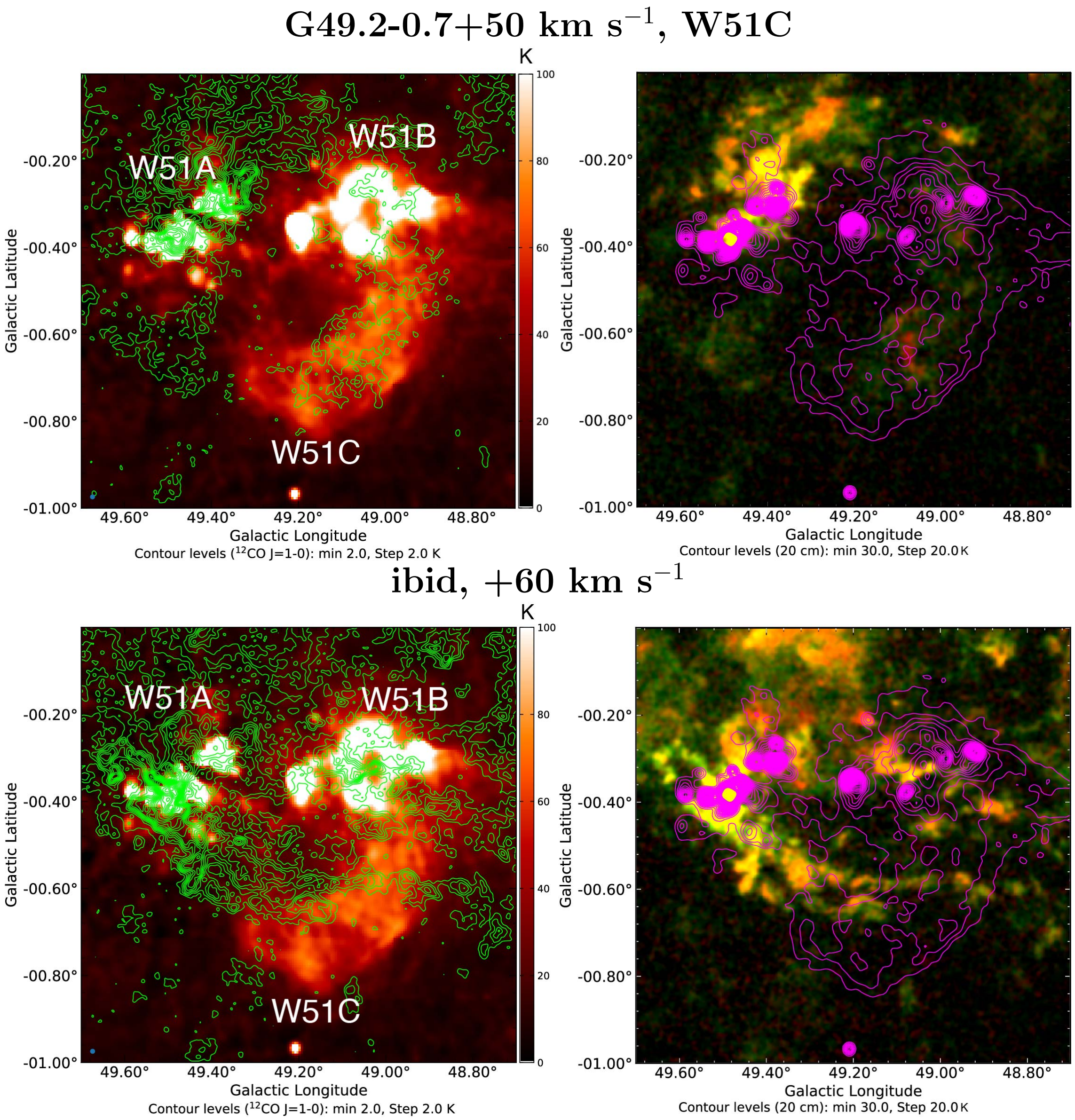

Figure 48. Same as figure 30, but for SNR G49.2-0.7; 50 and 60 km s^{-1}.

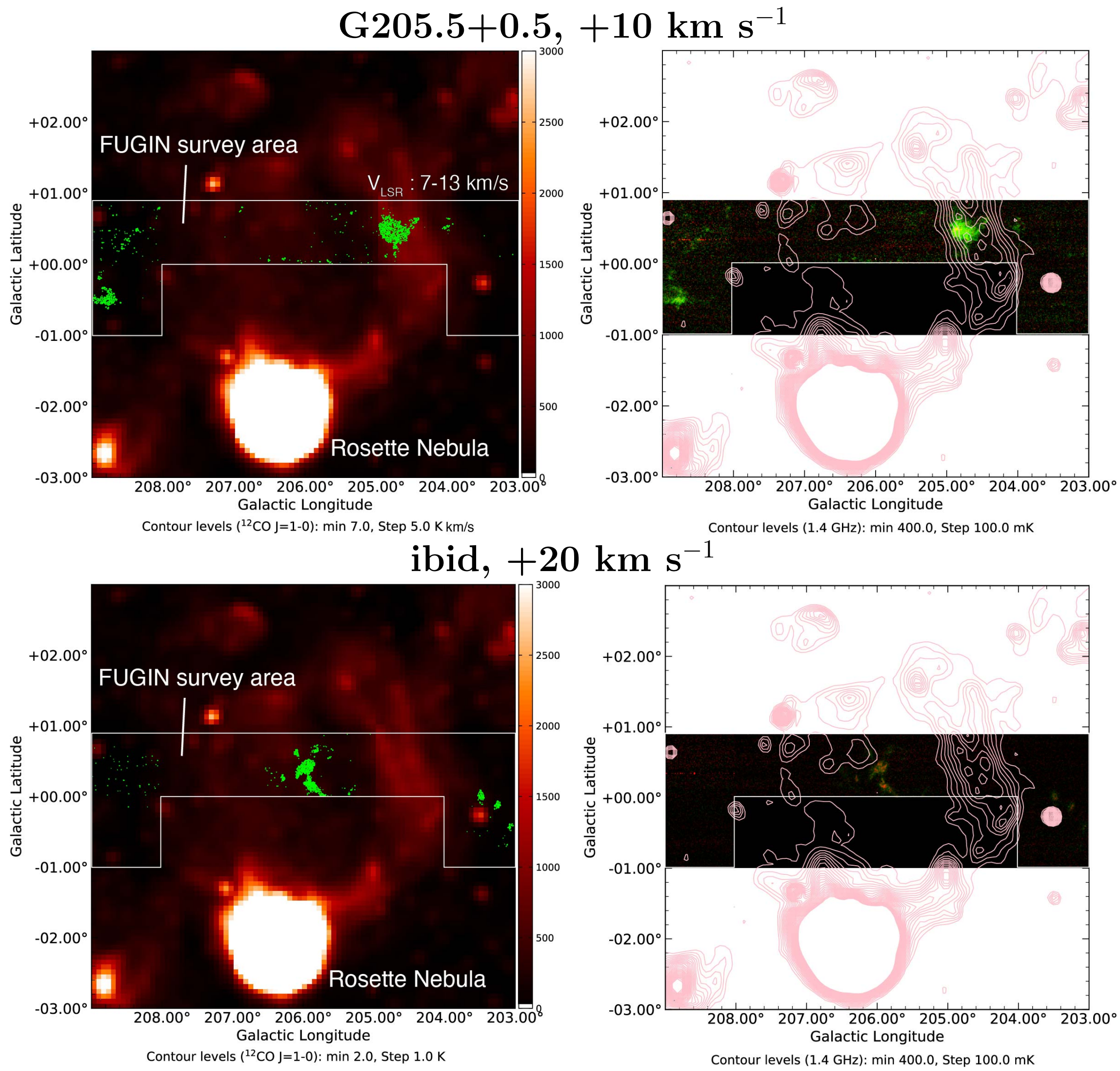

Figure 49. Same as figure 30, but for SNR G205.5+0.5, at 10 and 20 km s^{-1}. White line shows the observing area of the FUGIN CO survey. The radio continuum data is obtained by the Effelsberg 100 m telescope.

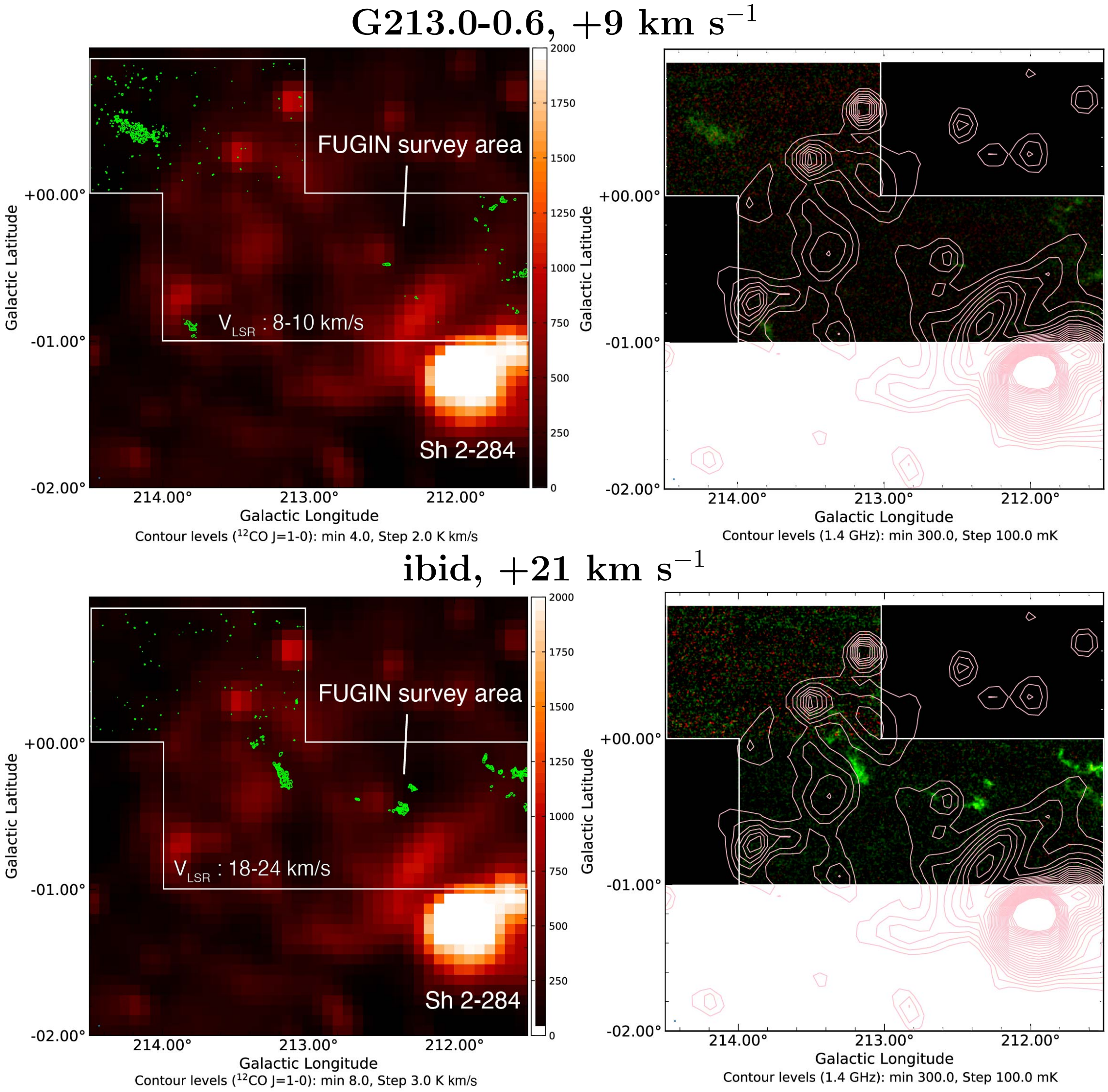

Figure 50. Same as figure 30, but for SNR G213.5-0.6; 9 and 21 km s^{-1}. White line shows the observing area of the FUGIN CO survey. The radio continuum data is obtained by the Effelsberg 100 m telescope.